An efficient approach to capture continuous impervious surface dynamics using spatial-temporal rules and dense Landsat time series stacks

Chong Liu[a,b], Qi Zhang[c,*], Hui Luo[d], Shuhua Qi[a,b], Shiqi Tao[e,f], Hanzeyu Xu[g], Yuan Yao[h,*]

[a] *Key Laboratory of Poyang Lake Wetland and Watershed Research (Ministry of Education), Jiangxi Normal University, Nanchang 332000, PR China*
[b] *School of Geography and Environment, Jiangxi Normal University, Nanchang 332000, PR China*
[c] *The Frederick S. Pardee Center for the Study of the Longer-Range Future, Boston University, Boston, MA 02215, USA*
[d] *School of Computer Science, China University of Geosciences, Wuhan 430074, PR China*
[e] *Center for Global Change and Earth Observations, Michigan State University, East Lansing, MI 48824, USA*
[f] *Department of Geography, Environment, and Spatial Sciences, Michigan State University, East Lansing, MI 48824, USA*
[g] *Key Laboratory of Virtual Geographic Environment (Ministry of Education), Nanjing Normal University, Nanjing 210023, PR China*
[h] *Institute of Future Cities, The Chinese University of Hong Kong, Shatin, Hong Kong*

ARTICLE INFO

ABSTRACT

Impervious surface dynamics have far-reaching consequences on both the environment and human well-being. The expansion of impervious surface is often spontaneous and conscious, particularly in fast developing regions. Thus, monitoring impervious surface dynamics with high temporal frequency in a both accurate and efficient manner is highly needed. Here, we propose an approach to capture continuous impervious surface dynamics using spatial-temporal rules and dense time series stacks of Landsat data. First, a stable area mask based on image classification in the start and the end years is generated to remove pixels that are persistent or spatially irrelevant. The Continuous Change Detection (CCD) algorithm is then employed to determine the change points when non-impervious cover converts to impervious surface based on the property of temporal irreversibility. Finally, the CCD time series models are calibrated for pixels with no change or multiple changes. We apply and assess the proposed approach in Nanchang (China), which has been experiencing rapid impervious surface expansion during the past decade. According to the validation results, overall accuracies of image classification in the start and the end years are 97.2% and 96.7%, respectively. Our approach generates convincing results for impervious surface change detection, with overall accuracy of 85.5% at the annual scale, which is higher than three commonly used approaches in previous studies. At the continuous scale, the mean biases of the detected time of imperviousness emergence are $+0.17$ (backward) and -3.42 (forward) Landsat revisit periods (16 days) for pixels with one single change and multiple changes, respectively. The derived impervious surface extent maps exhibit comparable performances with five widely used products. The present approach offers a new perspective for providing timely and accurate impervious surface dynamics with dense temporal frequency and high classification accuracy.

1. Introduction

The Earth's terrestrial surface has been drastically urbanized under rapid economic development and population growth. The percentage of global urban population is expected to exceed 60% by 2050 (UN, 2014) and approach 100% by 2092 (Batty, 2011). The demand for land space for urban human life has never been greater. As a key characteristic of urbanization, the expansion of impervious surface will also continue to intensify, giving rise to pressure on the environment worldwide (Grimm et al., 2008; Seto et al., 2012; Weng, 2012).

Impervious surfaces, such as rooftops, sidewalks and paved roads, refer to land cover types that prevent water filtration into soil (Arnold Jr and Gibbons, 1996). Impervious surface expansion not only indicates the process of urbanization, but also manifests anthropogenic features that affect environmental change (Weng, 2012). Increase in impervious cover can influence land surface conditions in multiple ways, such as modifying surface runoffs with frequent floods (Brun and Band, 2000), transporting non-source pollution (Hurd and Civco, 2004), and increasing land surface temperature through the urban head island effect (Yuan and Bauer, 2007). Thus, tracking impervious surface dynamics is

of crucial relevance to understanding urbanization impacts on eco-hydrological processes (Boggs and Sun, 2011; Hao et al., 2015), climate change (Deng and Wu, 2013), and human health (Gong et al., 2012). Moreover, it propels the engagement of policy-makers in better resource management and urban sustainable development, especially in fast developing countries or regions where such data are commonly unattainable (Gong et al., 2016).

Monitoring impervious surface expansion has been difficult because it often follows a nonlinear trend with high spatial and temporal heterogeneity (Sexton et al., 2013). The advent of satellite remote sensing offers unique advantages for studying such dynamics. Previous approaches for impervious surface change detection based on remotely sensed imagery can be categorized into pre-classification and post-classification (Singh, 1989). The pre-classification technique directly classifies stacked images with different dates and regards each change type as an independent class (Seto et al., 2002; Gao et al., 2012; Schneider, 2012). Although this technique is capable of producing temporally consistent impervious surface maps, its sample collection requires not only land cover labels but also change type and duration, making it difficult to obtain sufficient high-quality reference data for model training and validation (Wu et al., 2017). The post-classification analysis classifies each image individually and then derives "from-to" information via per-pixel comparison (Singh, 1989; Olofsson et al., 2013). This technique is widely used in the literature (Bagan and Yamagata, 2012; Qin et al., 2017). However, it neglects the inherent correlation of the classified impervious surface sequence, making additional treatments necessary before change detection (Wu et al., 2017).

Currently, impervious surface areas occupy only 0.2–2.7% of the total earth terrestrial land (Schneider et al., 2010; Song et al., 2016; Liu et al., 2017), its associated land cover changes being even smaller. Thus, much effort would be saved if spatially irrelevant areas were removed before impervious surface change detection. This also alleviates spectral confusion between land cover classes that exhibit similar characteristics, enhancing classification accuracy (Li and Gong, 2016). The 2006 National Land Cover Database Impervious Surface Products (NLCD Imperviousness 2006) is an example of such an attempt. Specifically, changed and unchanged areas are first separated based on the 2001 product (NLCD Imperviousness 2001) and new impervious surface areas are then predicted in only the changed areas (Xian and Homer, 2010). This algorithm serves as a baseline for developing more sophisticated methods for impervious surface change detection (Yu et al., 2016; Wu et al., 2017; Li et al., 2018).

It becomes clearer that denser temporal frequency is key to studying the evolving nature of urban land cover and land use patterns. However, a major limitation of existing impervious surface products pertains to the relatively long temporal intervals. Such products as the widely used NLCD Imperviousness (updated every five years) can no longer meet the needs of understanding urbanization processes because impervious surface growth can often be conscious or spontaneous (Chen et al., 2014). Thus, researchers have endeavored to improve methods of multi-temporal impervious surface change detection by generating more frequent observations. Li et al. (2015) used Landsat data to map urban dynamics of Beijing (China) during 1984–2013 at an annual frequency. More recently, Zhang et al. (2017) created monthly impervious cover maps of the Pearl River Delta by fusing Landsat and MODIS time series data. Both studies adopted the post-classification technique for change detection, requiring additional steps such as temporal consistency check to refine the classification results. Moreover, it can be extremely laborious to classify each individual image for a long time series or in a large area. Due to this dilemma, it is still needed to improve the temporal mapping technique of impervious cover regarding both efficiency and accuracy.

The expansion of impervious surface is the most irreversible process among all land cover changes (Gao et al., 2012; Seto et al., 2011; Mertes et al., 2015; Schneider and Mertes, 2014; Li et al., 2015; Zhang and Weng, 2016), particularly in developing regions where urbanization is

at the booming stage. Based on this premise, two assumptions can be derived. First, the conversion from non-impervious cover to impervious surface is unidirectional, meaning that the inverse process is unrealistic and should be avoided. Second, the existing impervious surface area will persist in the subsequent years. Following these spatial-temporal rules, mapping impervious surface dynamics can focus only on where the newly emerged impervious surface areas are and when their associated land cover changes occurred. Spatially, irrelevant areas such as land cover changes between impervious surfaces (e.g., from sideway to rooftop) and between non-impervious covers (e.g., from forest to cropland) can be identified and removed before change detection analysis. Temporally, monitoring continuous impervious surface dynamics can be simplified by detecting the change point from non-imperviousness to imperviousness via time series analysis. Although straightforward, few studies directly leverage the spatial-temporal rules, which is due primarily to two difficulties. The first is the lack of data availability. Acquiring and pre-processing satellite imagery data used to be laborious and expensive. Unfavorable atmospheric conditions such as snow, cloud, and cloud shadow further reduce the number of clear observations (Zhu et al., 2015). This issue becomes even more critical when involving large spatial and temporal extents. The second difficulty is the lack of appropriate algorithms. Traditional approaches of detecting impervious surface changes are usually image or scene oriented, which are constrained by satellite sensors. Temporal profile analysis, however, requires extending the temporal scale beyond that of the sensors.

The open availability of all Landsat archived data has revolutionized our way of monitoring land cover and land use change (Woodcock et al., 2008; Liu et al., 2018a; Wulder et al., 2018; Zhu et al., 2019a). The mass of satellite records has promoted the development of specialized algorithms of time series change detection with multiple applications, such as BFAST (Verbesselt et al., 2012), LandTrendr (Kennedy et al., 2010), and VCT (Huang et al., 2010). Among all the algorithms, Continuous Change Detection and Classification (CCDC) has exhibited great potential of identifying land disturbance through time (Zhu and Woodcock, 2014; Pengra et al., 2016; Zhu et al., 2019b). It has been widely used in studying the dynamics of the terrestrial environment, including deforestation (Olofsson et al., 2016; Zhu et al., 2016b), urban greenness change (Zhu et al., 2016a), and impervious surface expansion (Deng and Zhu, 2018).

The present study aims to develop an efficient approach for capturing continuous impervious surface dynamics based on the spatial-temporal rules. The term "continuous" means that an impervious surface extent map at any given time during the study period can be obtained. To achieve this goal, we adopt the CCDC algorithm and use dense time series stacks of Landsat data for impervious surface change detection. We test the proposed approach in Nanchang, China, a city characterized by rainy climate, heterogeneous landscape and rapid impervious surface growth, over the study period of 2002–2016.

2. Study area and data source

2.1. Study area

The study area is Nanchang City (28°10′-29°11′N, 115°26′-116°34′E), China, which covers an area of 7194 km² in the middle and lower reaches of the Yangtze River with a population of approximately 5.30 million (Jiangxi Statistics Yearbook, 2017). The boundary of Nanchang encompasses nine administrative districts/counties and spans two Worldwide Reference System-2 (WRS-2) scenes (Fig. 1). Among the nine districts, four (Donghu, Xihu, Qingyunpu, and Qingshanhu) are located in the center of Nanchang and regarded as the downtown area or the urban core, while the other five in peripheral regions are characterized mostly by peri-urban or rural areas. We select Nanchang as the study area for two main reasons. First, Nanchang exemplifies many other cities in China that have been experiencing
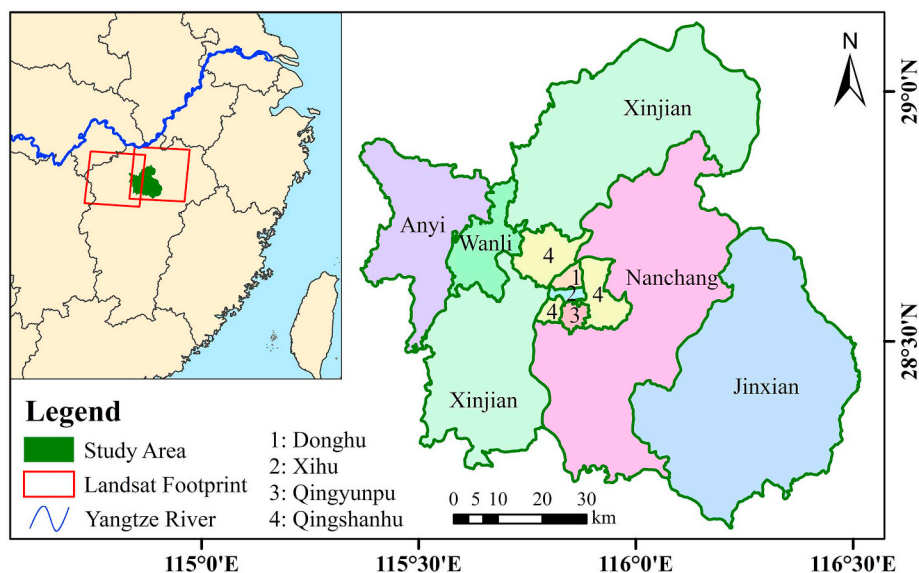
Fig. 1. Location of study area (Nanchang, China) and its administrative units at the district/county level.

phenomenal urbanization during the past decades. During 2000–2016, the city's population has increased by 11.57% (Jiangxi Statistics Yearbook, 2000–2017). At the same time, rapid industrialization and massive infrastructure construction have led to drastic land cover changes such as conversion from agricultural and natural lands to urban lands, which are accompanied with substantial impervious surface expansion. Second, the composition of land cover in Nanchang is highly heterogeneous. Such a variable and dynamic geographical environment offers a valuable opportunity to examine our approach of continuous change detection of impervious surface.

2.2. Landsat data

We accessed Collection 1 Level-2 Landsat data from U.S. Geological Survey (https://espa.cr.usgs.gov/) via the platform of Google Earth Engine (GEE), which is a cloud-based geospatial analysis platform with massive computational capabilities (Gorelick et al., 2017). We obtained all available Landsat 5, 7, and 8 images with identification indices of "LANDSAT/LT05/C01/T1_SR", "LANDSAT/LE07/C01/T1_SR", and "LANDSAT/LC08/C01/T1_SR", respectively, in GEE. We filtered the image collections by the extent of the study area (WRS-2 Path/Row 121/40 and 122/40) and study period (from 2002 to 2016). For each Landsat image, six surface reflectance bands, one thermal band and one quality assessment band were employed (Zhu et al., 2015; Zhu et al., 2016a). It should be noted that the C Function of Mask (CFMask) algorithm (Zhu and Woodcock, 2012; Zhu et al., 2015) has been incorporated in the quality assessment band so that poor quality observations, including fill, snow, cloud and cloud shadow, have been labeled, leaving the remaining clear observations. Landsat Collection 1 (https://landsat.usgs.gov/landsat-collections) consists of three categories, including Tier 1, Tier 2, and Real-Time. We used data only in Tier 1 because they meet the formal quality criteria and thus are most suitable for time series analysis. In total, 719 Landsat scenes were included. Among these scenes, Landsat 7 has the largest number of scenes, followed by Landsat 5, and Landsat 8 the least (Fig. 2a). The spatial distributions of total observations, clear observations, and clear observation percentages for all Landsat scenes are shown in Fig. 2b-d.

2.3. Auxiliary data

In this study, we use several auxiliary data in addition to Landsat time series images. Very High Resolution (VHR) imagery was obtained

from Google Earth and historical orthophotos provided by Department of Natural Resource of Jiangxi Province. Vector data of administrative township/village boundaries were acquired from National Geomatics Center of China. Global inter-calibrated nighttime lights (NTLs) data (Zhang et al., 2016) were provided by Yale University (https://urban.yale.edu/data).

3. Methods

Fig. 3 shows the flow chart of the proposed approach, which includes two major stages, spatial masking of stable area and temporal change detection analysis. First, we exclude areas that are temporally persistent or characterized by irrelevant land cover changes. This procedure is implemented by independent land cover classification in the start and end years. Second, we perform a per-pixel change detection analysis for the remaining areas to detect when and where non-impervious land cover convert to impervious surface. Detailed procedures of the approach are described below.

3.1. Creation of stable area mask

According to the irreversibility assumption, impervious surface expansion during the study period should be bounded by its initial and final states. Given the impervious surface extent maps in the start and end years (i.e., 2002 and 2016), all image pixels can be divided into 1) target pixels where the transition from non-imperviousness to imperviousness occurred, 2) persistent imperviousness, and 3) persistent non-imperviousness. Only target pixels were selected for further change detection (Fig. 4). This procedure not only saves unnecessary workload but also alleviates the confusion between impervious surface and other land cover types.

3.1.1. Feature extraction

To overcome the influence of cloud and cloud shadow, a pixel-based compositing approach (White et al., 2014) was applied before the classification procedure. This approach first calculates four scores for each pixel, including sensor score, day of year score, distance to cloud or cloud shadow score, and opacity score. A comprehensive total score is then generated as the sum of all these scores. The pixel with the highest comprehensive score is used as the composited output for the analysis. Since combining images from different seasons is advantageous in producing high classification accuracy (Dannenberg et al.,
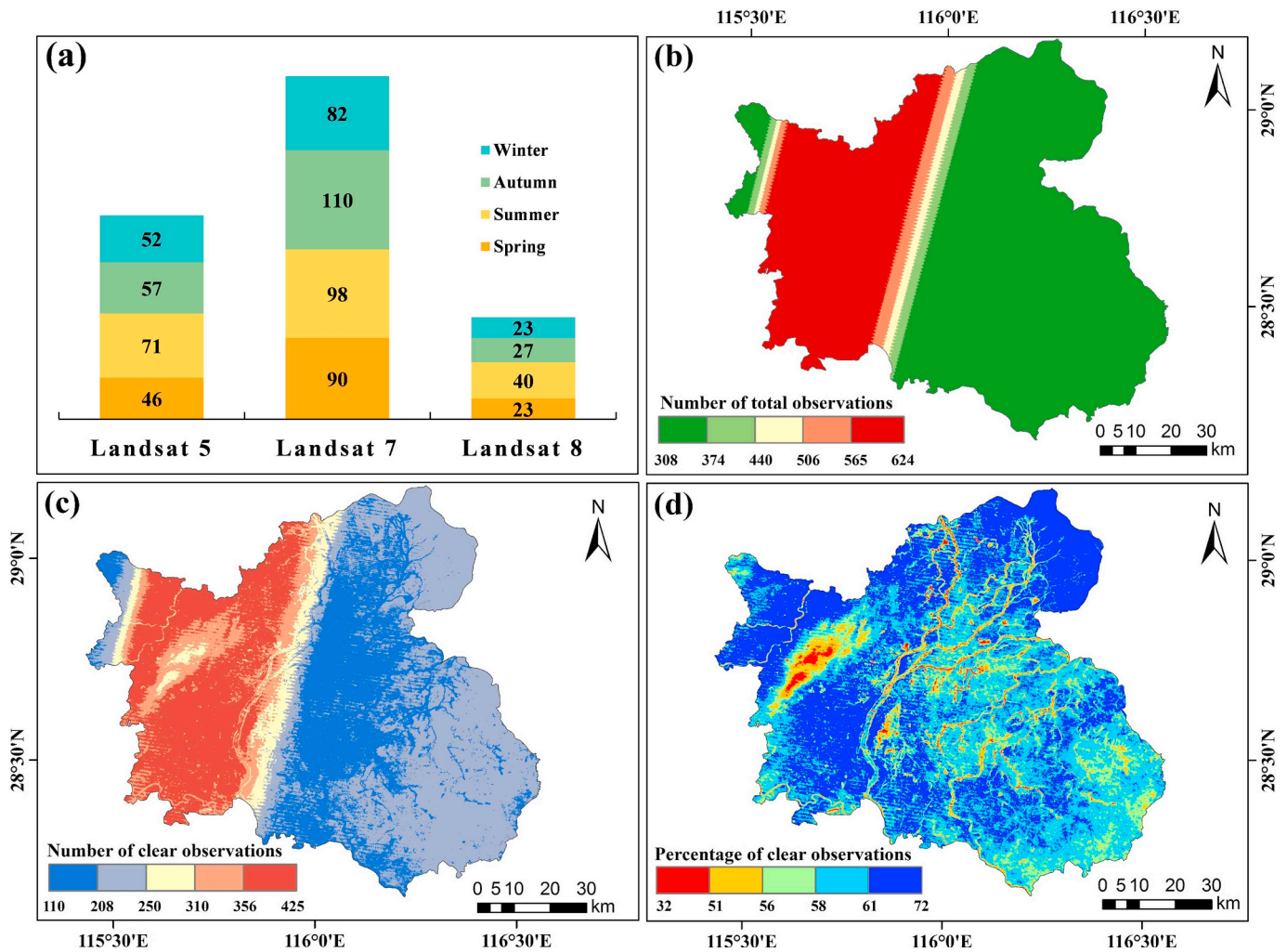
Fig. 2. Landsat 5–8 Collection 1 Level-2 products used in this study. (a) Sensor and seasonal distribution. (b)-(d) Spatial distributions of total observations, clear observations, and clear observation percentage, respectively.

2016; Zhu et al., 2012), we applied this compositing approach for each season and generated a multi-seasonal compositing set (spring, summer, autumn and winter) in 2002 and 2016, separately. From each compositing result, we extracted eight types of image features, including six surface reflectance (green, blue, red, NIR, SWIR1 and SWIR2) bands and two spectral indices, which are the Normalized Difference Vegetation Index (NDVI) (Tucker, 1979) and the modified Normalized Difference Water Index (mNDWI) (Xu, 2006). Eventually, a total of 32 feature bands were adopted for the single year classification.

3.1.2. Classification and mask generation

Based on the geographical environment of the study area, we designed a six-class scheme including impervious surface, bareland, cropland, forest, wetland and water. Training samples were collected through visual interpretation of VHR imagery and Landsat data acquired in 2002 and 2016, separately. Special care was taken to wetland because it is easily confused with other classes in spectral characteristics for a single season (e.g., bareland in winter and water in summer). Thus, images from continuous Landsat data were used to support VHR imagery interpretation as needed. For each year, we randomly generated 3500 training sample points. After visually cross-checking and removing pixels deemed incorrect, there remained 2931 sample points for the 2002 image, including 64, 1527, 832, 220, 151, 137 points for bareland, cropland, forest, impervious surface, wetland, and water, respectively, and 3119 sample points for the 2016 image, including 87,

1497, 837, 340, 222 and 136 points for bareland, cropland, forest, impervious surface, wetland, and water, respectively.

To create the land cover maps, Random Forest Classifier (RFC) was applied because it is robust in mapping large-area land cover and particularly effective when a large number of features is involved (Pal, 2005; Zhu et al., 2012; Gong et al., 2013; Zhang et al., 2018a). To balance computation time and classification performance, we implemented RFC with 500 trees and the square root of the total number of input variables as the number of variables to split each node. Note that the initial output of RFC for each year was a six-category land cover map. The six land covers were re-classified into impervious surface and non-impervious surface.

3.1.3. Accuracy assessment for classification

The accuracy assessment for each of the impervious surface classification in 2002 and 2016 was conducted in two ways. In the first validation method, 2000 stratified random samples were independently selected from the classification result, with one half collected from impervious surface areas while the other half from the non-impervious areas (Li and Gong, 2016). Based on these validation samples, we obtained the confusion matrix and calculated quantitative metrics including overall accuracy (OA), Kappa coefficient, producer's accuracy (PA) and user's accuracy (UA). Previous studies suggested that using only confusion matrix may not be sufficient to evaluate the performance of mapping impervious surface, particularly in peri-urban and
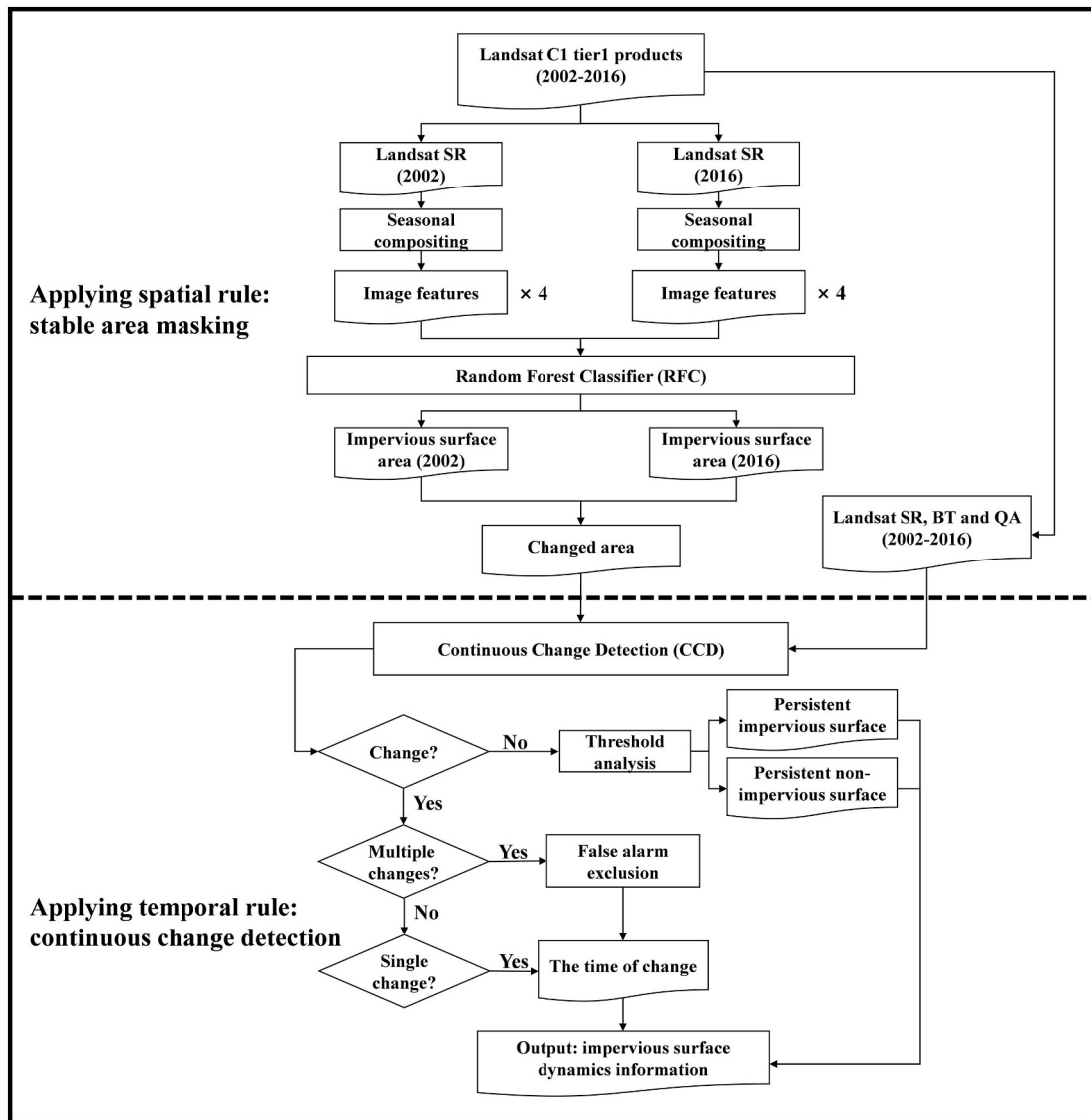
Fig. 3. Flow chart of the proposed approach for tracking continuous impervious surface dynamics. SR, BT and QA denote surface reflectance, brightness temperature and quality assessment, respectively.

rural areas where settlements are highly fragmented (Schneider, 2012; Qin et al., 2017). Thus, we conducted a second validation method by testing the classified map regarding the presence/absence of impervious surface clusters outside of the downtown areas (i.e., the five districts in peripheral areas of Nanchang) against reference data conjunctively collected from VHR imagery and administrative village distribution data. Specifically, we randomly selected 60 test clusters, each of which is comprised of at least two contiguous pixels of imperviousness, and created a 3-km circle buffer for each cluster. Then, we enumerated all impervious surface clusters within each buffer for both the classified map and the reference data (Schneider, 2012). We finally used scatter plots of the cluster numbers and their fitted lines to validate the mapped impervious surface. The above-mentioned assessments were conducted for the two epoch classification results, separately.

3.2. Continuous change detection

3.2.1. The CCD algorithm

The CCDC algorithm assembles all available Landsat observations for each pixel to estimate time series models and uses the models to predict future observations (Zhu and Woodcock, 2014; Zhu et al.,

2015). A break will be labeled if the values of new consecutive observations are out of the expected range, and a new time series model will be estimated until the next break is detected or the observations are exhausted. The time series models are composed of Fourier models so that both intra-annual (phenological) and inter-annual (gradual) changes can be identified. A detected break indicates an abrupt change of the land surface environment, which is usually caused by land use and land cover change. The algorithm further classifies a pixel to identify the land cover types before and after a break occurs.

In this study, we used only the change detection component of CCDC (https://github.com/USGS-EROS/lcmap-pyccd) to derive land cover change information for continuous impervious surface dynamic analysis. Thus, it was renamed CCD hereafter. We used default parameters for running the CCD algorithm, namely 0.99 change probability, 6 consecutive observations, and a maximum of 8 coefficients for the time series models. Since CCD requires several observations to initialize the algorithm, we recorded the start and end times of the entire time series for each pixel, which define the interval of the time series model.

3.2.2. Change detection analysis

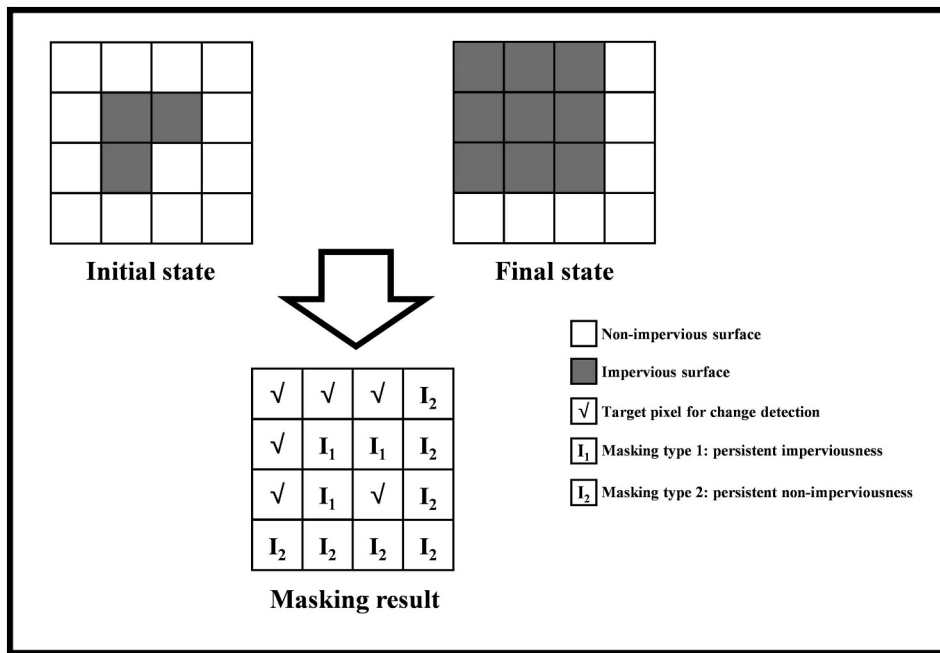Once the time series models were estimated by CCD, the per-pixel

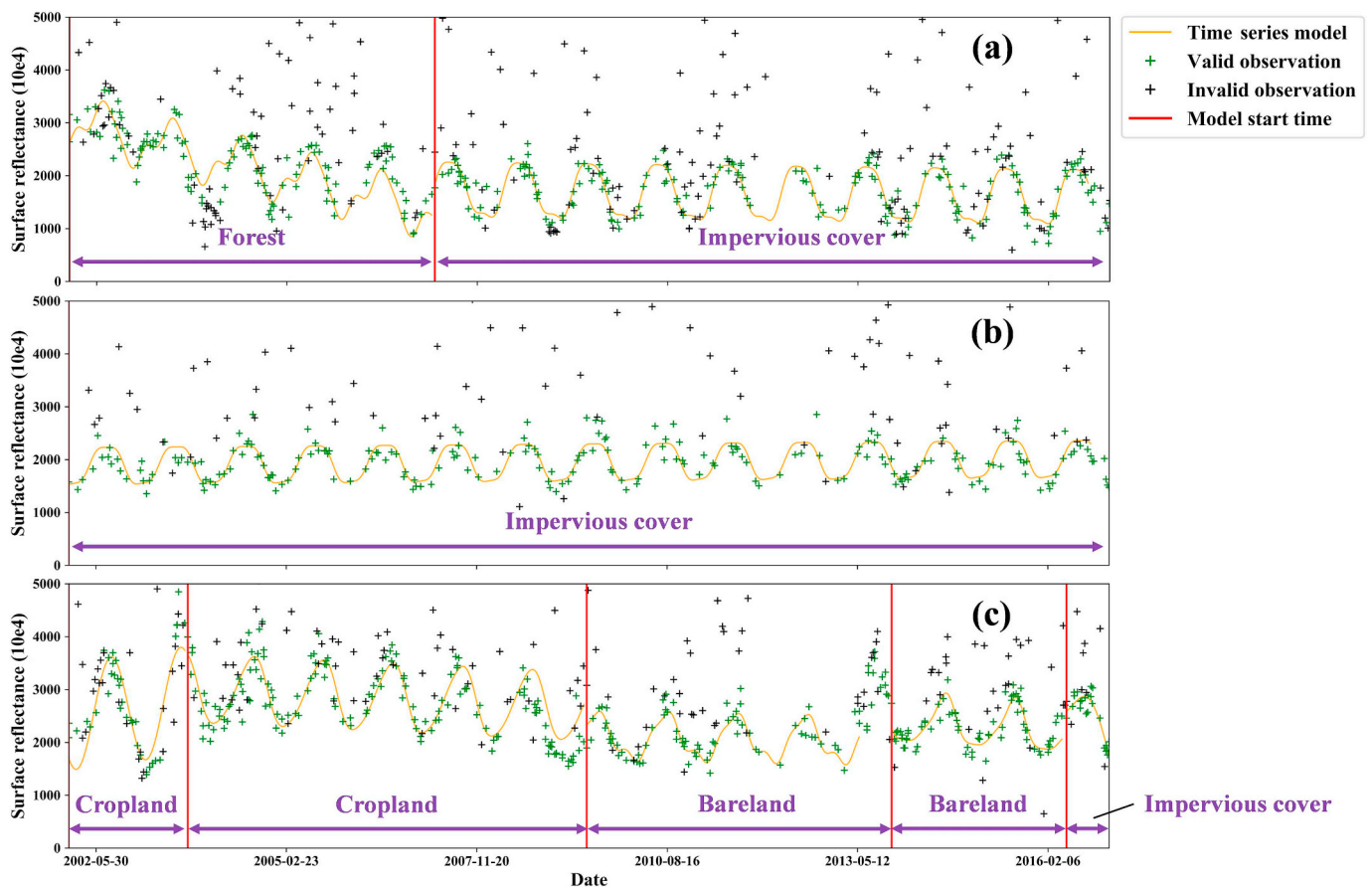**Fig. 4.** Illustration of the spatial masking process.

Fig. 5. Three scenarios in change detection analysis with (a) one single abrupt change, (b) no abrupt change, and (c) multiple abrupt changes. Only the NIR band is displayed. Invalid observations (fill, snow, cloud and cloud shadow) are identified by the quality assessment (QA) band.

change detection analysis can be conducted. Fig. 5 demonstrates three scenarios under which impervious surface dynamics are modeled by CCD for each pixel. In the first scenario, the pixel changes only once and thus two time series models are estimated (Fig. 5a). By identifying the

time point of the break, we can determine when the pixel changed from non-impervious cover to impervious surface. It should be noted that there might exist a short "disturbed" period between the two estimated models due to the large spectral variability, in which case we define the

start date of the latter model as the time point that separates the two estimated models (Zhu et al., 2015).

In the second scenario, no break is recorded and thus only one single time series model was estimated (Fig. 5b). In other words, the pixel does not experience any land disturbance throughout the entire period and is identified as a "persistent" pixel. Since stable areas have been excluded in the masking procedure, "persistent" pixels could be due to classification errors and thus should be corrected. For the purpose of validation and correction (see Section 3.2.3), we developed a threshold-based approach to separate persistent impervious and non-impervious pixels identified by CCD. Given that impervious surfaces are positively correlated with land surface temperature and negatively correlated with NDVI (Zhang et al., 2017), an index K can be defined as:

$$K = \frac{BT}{NDVI} \tag{1}$$

where BT is the brightness temperature derived from the thermal band. We then calculated the mean values of impervious surfaces ($\overline{K}_{imp}$) and non-impervious surfaces ($\overline{K}_{non}$) using all training samples. For pixel (x,y), the equation of identifying its class can be written as:

$$IMP_{(x,y)} = \begin{cases} 1, |K_{(x,y)} - \overline{K}_{imp}| < |K_{(x,y)} - \overline{K}_{non}| \\ 0, \text{otherwise} \end{cases} \tag{2}$$

where $IMP_{(x,y)}$ is the final binary result, with "1" denoting persistent imperviousness and "0" persistent non-imperviousness.

The third scenario illustrates a more complex land conversion case in which multiple breaks are detected (Fig. 5c). This could happen because of two reasons. First, land conversions between non-impervious covers (e.g., a break where forest changed to bareland due to clear-cutting) occur before impervious surfaces eventually emerge. Second, intra-transformation between different types of impervious surface (e.g., from pavement to building) can also be detected and identified as a break by CCD. Therefore, the aim here is to detect the "true" change time when natural covers were converted to impervious surfaces by excluding the breaks with "false" alarms. Fig. 6 illustrates the procedure of false alarm exclusion for a pixel. Given time series models $M = \{M_1, M_2, …, M_n\}$, their start times and periods can be obtained and expressed as $T = \{T_1, T_2, …, T_n\}$ and $P = \{P_1, P_2, …, P_n\}$, respectively. The entire study period can be divided into two parts, including a pre-change period with non-impervious cover and a post-change period with impervious surface. Since impervious cover, as mentioned above, tends to exhibit higher land surface temperature but lower NDVI than non-

impervious cover (Zhang et al., 2017), we can expect that the value of K for the post-change period reaches the maximum when the whole study interval is correctly separated. Therefore, the aim is to find the time point T_i when an objective function O_{T_i} can be maximized. The equation of the objective function can be written as:

$$O_{T_i} = \frac{BT_{T_i}^{post}}{NDVI_{T_i}^{post}}, i \in [2, n] \tag{3}$$

where n denotes the times of change during the entire study period, while $BT_{T_i}^{post}$ and $NDVI_{T_i}^{post}$ are the average brightness temperature and NDVI fitting values, respectively, during the post-change period determined by T_i. They can be calculated as:

$$BT_{T_i}^{post} = \frac{1}{\sum_{l=i}^{n} P_l} \sum_{l=i}^{n} \sum_{j=T_l}^{T_l+P_l-1} BT\_fit_j^{nor} \tag{4}$$

$$NDVI_{T_i}^{post} = \frac{1}{\sum_{l=i}^{n} P_l} \sum_{l=i}^{n} \sum_{j=T_l}^{T_l+P_l-1} NDVI\_fit_j^{nor} \tag{5}$$

where $BT\_fit_j^{nor}$ and $NDVI\_fit_j^{nor}$ are normalized brightness temperature and NDVI fitting values, respectively, at Julian date j. They can be obtained as:

$$BT\_fit_j^{nor} = \frac{BT\_fit_j - BT\_fit^{min}}{(BT\_fit^{max} - BT\_fit^{min})} \tag{6}$$

$$NDVI\_fit_j^{nor} = \frac{NDVI\_fit_j - NDVI\_fit^{min}}{(NDVI\_fit^{max} - NDVI\_fit^{min})} \tag{7}$$

where BT_fit_j and $NDVI\_fit_j$ are model fitted brightness temperature and NDVI values, respectively, at Julian date j; BT_fit^{max}, BT_fit^{min}, $NDVI\_fit^{max}$ and $NDVI\_fit^{min}$ are modeled maximum and minimum values of brightness temperature and NDVI, respectively, during the whole study period.

3.2.3. Accuracy assessment for change detection and error-adjusted area estimates

We used continuous Landsat data themselves as the primary source for change detection performance validation because currently no other reference data can provide comprehensive change detection assessment both temporally and spatially (Zhu et al., 2015). Visual interpretation of continuous Landsat time series from all seven bands facilitated the process of identifying the time of land cover change occurrence. VHR
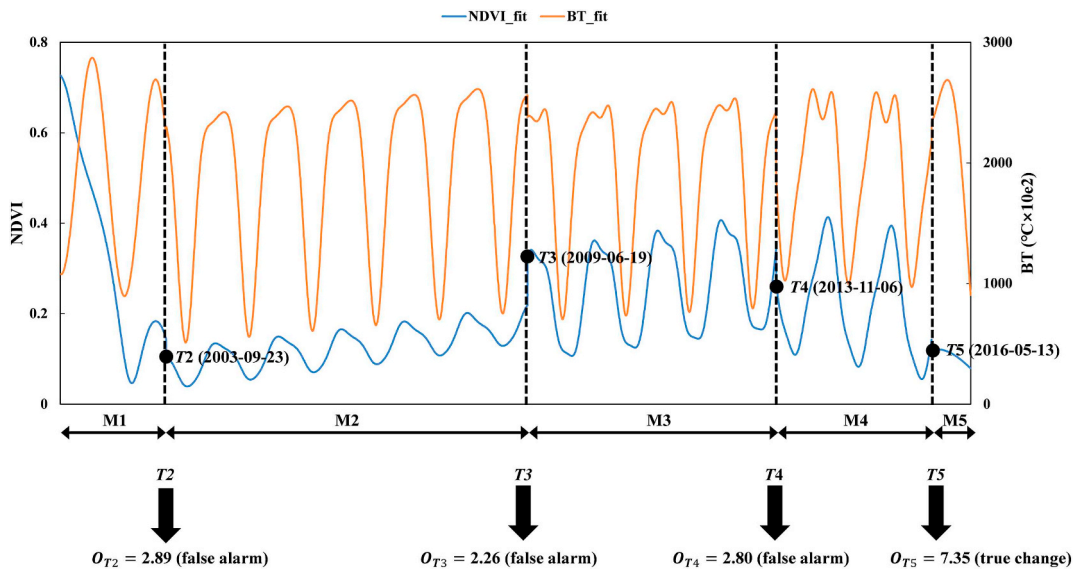

Fig. 6. False alarm exclusion for pixels with multiple abrupt changes. M1-M5 represent five CCD derived time periods. NDVI_fit and BT_fit represent fitted NDVI and thermal time series, respectively. Abrupt changes (T2-T5) are displayed as black dots.

Table 1
Class scheme for validating change detection performance.

Category	T_{2002}	T_{2003}	…	T_i	…	T_{2015}	T_{2016}	Description
Non-imp	0	0	0	0	0	0	0	Persistent non-impervious cover
2003	0	1	1	1	1	1	1	Impervious cover since 2003
2004	0	0	1	1	1	1	1	Impervious cover since 2004
…	…	…	…	…	…	…	…	…
2015	0	0	0	0	0	1	1	Impervious cover since 2015
Imp	1	1	1	1	1	1	1	Persistent impervious cover

Note: T_i denotes land cover label as non-impervious (0) or impervious (1) in Year *i*.

imagery was used to refine the judgements. We employed a stratified random sampling scheme to collect independent validation samples (Gao et al., 2012). As illustrated in Table 1, we stratified all unmasked pixels into 15 classes based on the predicted time points of change from non-impervious to impervious cover, and randomly selected 40 sample points from each class (a total of 600 points) for change detection validation.

After acquiring the validation samples, we evaluated the change detection performance at two temporal scales, which are the annual scale and the continuous scale. At the annual scale, we derived the confusion matrix based on the 15 classes identified in Table 1. We compared our validation results to those derived from three previously published approaches on impervious surface change detection, including 1) post-classification without temporal consistency check (Post-1 approach), 2) post-classification with temporal consistency check (Post-2 approach), and 3) the original CCDC algorithm. Detailed descriptions of the three approaches are provided in Appendix A. At the continuous scale, we used only the samples where changes were detected by CCD to calculate their temporal biases (Zhu and Woodcock, 2014). The temporal bias is defined as the difference of land cover change time between our modeled outputs and the reference results. In this way, we evaluated not only the relative error of the estimated time point of change but also the overall tendency of forward or backward bias. Since we conducted false alarm exclusion for pixels with multiple changes, this validation approach was performed separately for pixels with one single change and multiple changes.

We further used the 600 validation samples to correct our annual impervious surface area estimates as well as to quantify their uncertainties (Olofsson et al., 2013; Li et al., 2015; Zhu et al., 2016a). We first re-classified the samples depending on the year of interest. For example, if we aimed to estimate the expanded impervious surface area before and after the year of 2010, the validation samples would be re-assigned into four categories, which are persistent impervious surface, persistent non-impervious surface, impervious surface emerged before 2010, and impervious surface emerged after 2010. Then, a confusion matrix was built based on this classification scheme. Finally, we followed the method described by Olofsson et al. (2013) to obtain the corrected impervious surface area estimate and its associated uncertainties (i.e., 95% confidence interval).

3.3. Creation of impervious surface maps and comparison with existing products

After acquiring the impervious surface extent at the initial stage (the year of 2002) and the per-pixel distribution of new imperviousness emergence, an impervious surface map at any given time within the study period can be generated. We further examined the generated impervious surface maps by comparing them with contemporary impervious surface products. In this study, we selected five well-established datasets, including GLC30, FROM-GLC, GHS, CAS-NLCD and NUACI (Table 2). These products were chosen because 1) they are widely used and include impervious surface (or homologous classes such as built-up or human settlement) as an independent land cover type; 2) they have relatively fine spatial resolutions comparable to that

of the Landsat products. We selected a fixed day of the year (December 31st) to generate the multi-epoch impervious surface maps. The inter-comparisons were then implemented at two stages. First, we compared our error-adjusted results with the reference products in terms of total impervious surface area statistics in different years. Second, we selected the year of 2010 (most products are available) to evaluate the impervious surface mapping performance with visual interpretation.

4. Results

4.1. Classification and stable area mask

As shown in Table 3, the classifications of impervious and non-impervious surfaces of Nanchang in 2002 and 2016 both have high accuracies, with OAs of 97.2% (kappa = 0.943) and 96.7% (kappa = 0.935), respectively. The total area of impervious surface in 2002 accounted for only 2.7% of Nanchang, while the percentage of impervious surface in 2016 increased to 7.5%. For impervious surface, in 2002, the PA (95.8%) is slightly lower than the UA (98.6%), suggesting a higher omission error than a commission error. In 2016, however, the PA (98.2%) of impervious surface is larger than the UA (95.2%).

Fig. 7 further reveals satisfactory classification performance in terms of the impervious surface clusters in peri-urban and rural areas of Nanchang in 2002 and 2016. Based on the reference data, our results explain over 94% of the sample variations in both years with tight fits to the 1:1 line, suggesting the impervious surface maps have correctly identified cluster numbers in most sites. In addition, the map of 2002 is found to have fewer impervious surface clusters, compared to the map of 2016.

Fig. 8 shows the classified land cover maps of Nanchang in 2002 and 2016, as well as the maps of stable and changed areas. In 2002, impervious surface areas were concentrated in the central Nanchang city, along the eastern shore of Ganjiang river, while the imperviousness clusters in relatively small pieces were scattered in the peri-urban and rural regions. In 2016, impervious cover in the urban core expanded to the peripheral regions, with greater spatial heterogeneity and various geometric structures due to the increased presence of mixed-used areas. The map of stable and changed areas (Fig. 8c) based on the classification shows that the conversion of cropland to impervious surface, which has occurred mainly on city outskirt, dominates the land cover changes in Nanchang during 2002–2016. The total area of impervious surface expansion is $345\,km^2$, accounting approximately 5% of the whole study area.

4.2. Change detection performance

To evaluate the performance of impervious surface change detection, we map three key outputs of the CCD time series models, including CCD start time, CCD end time and the number of abrupt changes during 2002–2016 (Fig. 9). For the changed pixels, CCD start times range from 2002-01-07 to 2002-12-26, with over 90% starting before 2002-09-30 (Fig. 9a). Comparably, CCD end dates, which range from 2016-01-15 to 2016-12-24, have a wider distribution (Fig. 9b). Spatially, the western

Table 2
Impervious surface products used for comparison.

Product	Spatial resolution (m)	Epoch used	Coverage	Approach	Source
GLC30	30	2010	Global	Pixel-Object-Knowledge (POK)-based	Chen et al. (2015)
FROM-GLC	30	2010, 2015	Global	Pixel-based	Gong et al. (2013); Yu et al. (2014)
GHS	~ 38	2014	Global	Pixel-based	Pesaresi et al. (2016)
CAS-NLCD	30	2005, 2010, 2015	China	Visual interpretation	Zhang et al. (2014)
NUACI	30	2005, 2010	Global	Rule-based	Liu et al. (2018b)

Table 3
Accuracy assessments for classification maps in 2002 and 2016.

Class	2002			2016		
	Area (%)	PA (%)	UA (%)	Area (%)	PA (%)	UA (%)
Impervious	2.7	95.8	98.6	7.5	98.2	95.2
Non-impervious	97.3	98.6	95.7	92.5	95.3	98.3
Both classes	OA = 97.2%, Kappa = 0.943			OA = 96.7%, Kappa = 0.935		

Note: PA, UA and OA are producer's accuracy, user's accuracy and overall accuracy, respectively.

part of the study area tends to have later end time than the eastern part. This is because the western part has the more available observations in the overlapped areas of two Landsat scenes. Based on these two results, we interpret and discuss further change detection performance by focusing on the years from 2003 to 2015. Fig. 9c, d show the spatial distribution and percentages of the numbers of no abrupt change, one single abrupt change, and multiple abrupt changes. Within the changed area, nearly half (49.81%) of the pixels have changed only once, while the proportion of pixels with no change accounts for only 7.84%. Meanwhile, the percentage of pixels with multiple changes (equal to or greater than two) is 42.35%, among which few changed more than three times (3.53%). Spatially, pixels with one single change are commonly found in all administrative districts/counties of Nanchang, while those with multiple changes are mainly distributed in the southern part of Nanchang County and northern part of Xinjian District.

To test if the index K effectively separates persistent impervious and non-impervious surface areas, we compare their frequency distributions (Fig. 10). Compared to non-impervious cover, impervious surface has a much wider distribution of K, suggesting greater heterogeneity in terms

of its spectral and thermal characteristics. The mean values of K for impervious and non-impervious surfaces are 23,042 and 4900 (4.36 and 3.69 in the logarithmic form), respectively, with their difference statistically significant ($|t| = 16.75$, $p = 0.000$). This indicates that the index performs well in differentiating persistent imperviousness from non-imperviousness.

Fig. 11 compares performances of impervious surface change detection at the annual scale between our approach and the three previously published approaches. Among all four approaches, our proposed approach exhibits the highest OA (85.5%), followed by the original CCDC (76.5%), while post-classification without temporal consistency check has the lowest OA (58.3%). Regarding the 15 categories described in Table 1, their PA and UA values substantially vary across all the four approaches. Compared to our approach, original CCDC has generally similar UAs but lower PAs, suggesting a larger omission error. This may be because that the original CCDC algorithm cannot well handle intra-class transformation of imperviousness and hence may produce illogical outputs for time series classification, such as conversion from impervious to non-impervious cover. The earlier the pixel changes from non-impervious to impervious surface, the more likely the original CCDC algorithm would detect a reversed conversion. This also explains why lower PAs tend to occur in the categories of early years (e.g., before 2011). The two post-classification approaches reveal both lower PAs and lower UAs than our approach and original CCDC. Post-classification with temporal consistency check generates higher PAs (Fig. 11b), since the post-treatment can correct some of the omission errors. However, such post-processes as the temporal consistency check may also raise additional commission errors, leading to lower UAs (Fig. 11a).

The continuous-scale accuracy assessment of the impervious surface change detection demonstrates that our predictions and the actual change dates are overall in good agreement (Fig. 12). The majority of
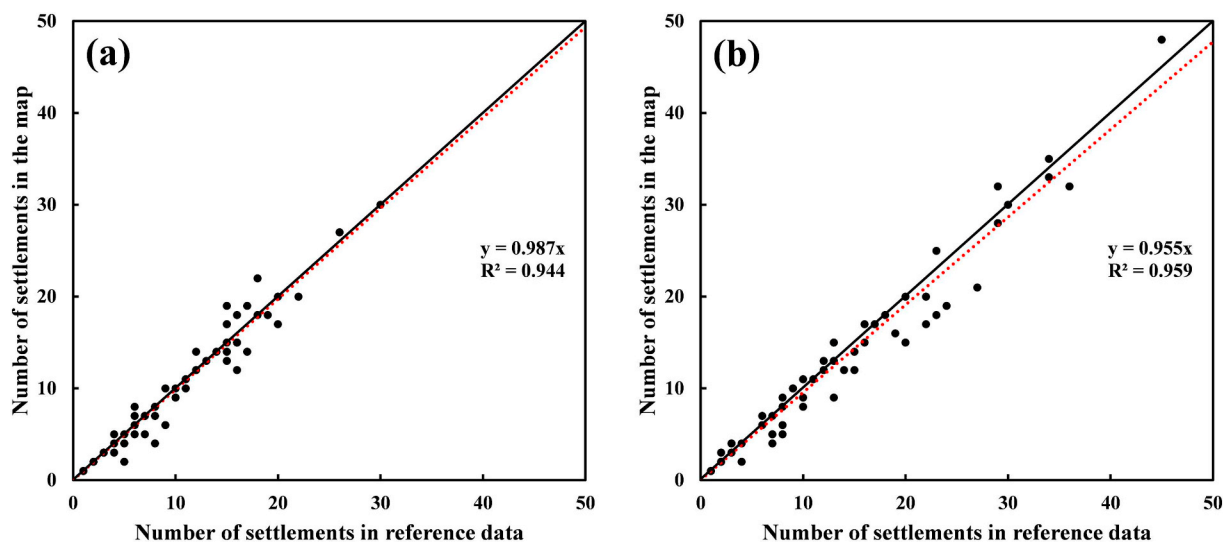

Fig. 7. Scatter plots of impervious surface cluster numbers derived from classification maps and reference data in 2002 (a) and 2016 (b). The black line is the 1:1 line. The red dot line is the linear fit with the intercept forced to 0. (For interpretation of the references to color in this figure legend, the reader is referred to the web version of this article.)
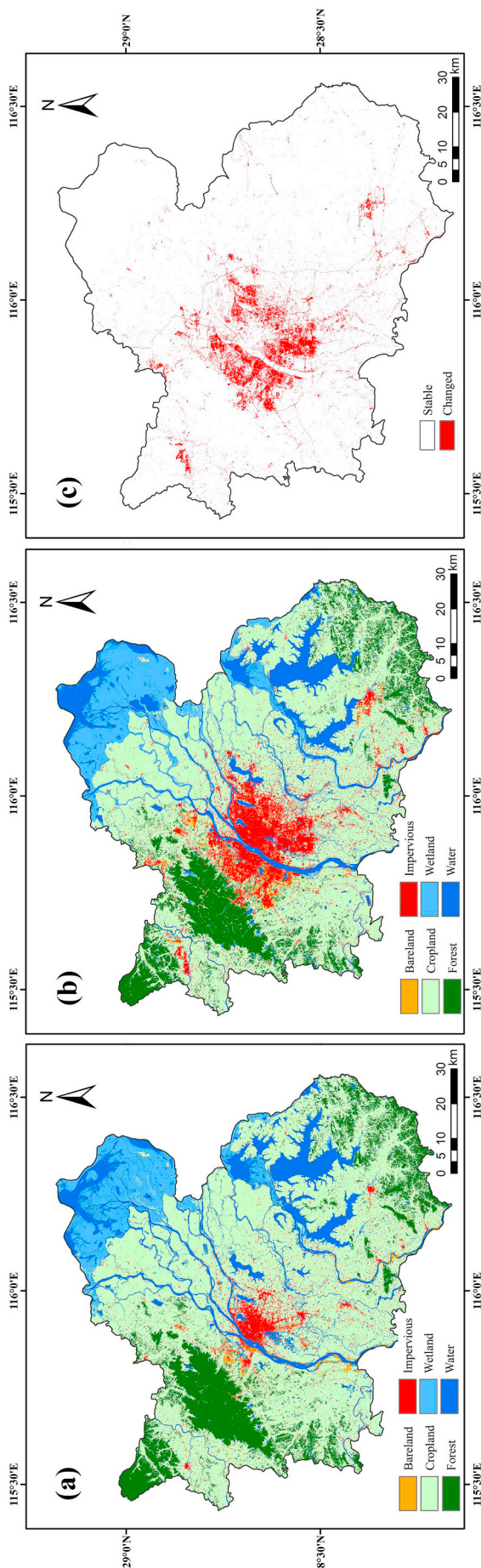
Fig. 8. Land cover classification and stable area mask. (a) Land cover map in 2002, (b) land cover map in 2016, and (c) map of stable and changed areas.

the samples have the same times of change as the reference data (i.e., bias = 0), with the proportions both above 70%. Grouped by the time of change, samples with one single abrupt change have a smaller mean bias (as well as standard deviation) than those with multiple abrupt changes. In addition, the two sample groups exhibit opposite temporal bias trends, and their mean biases are both within 3.5 Landsat revisit periods (56 days). Specifically, the mean biases are +0.17 and −3.42 with respect to one single change and multiple changes. The overall positive bias of the single change pixels can be explained by the fact that we used the start date of the latter time series model as the temporal boundary. As a consequence, the initial stage of change with partial impervious covers may be identified as the "disturbed" period (Zhu and Woodcock, 2014). Pixels with multiple changes, on the other hand, generally displayed a negative error trend, which may partially be due to that some false changes (e.g., conversion from forest to bright bare soil) are incorrectly identified as the "true changes".

Fig. 13 further shows two zoomed-in regions of the generated impervious surface maps, compared with the corresponding Google Earth VHR imagery, at three time points for visual evaluation. In the old town, impervious surface covers appeared steady during 2006–2015. Since this region has a railway hub characterized by massive infrastructures, available lands for impervious surface expansion was rather limited. On the contrary, a significant amount of increased impervious cover is observed in the new town district. From 2008-03-27 to 2010-09-20, the growing rate of impervious surface areas was slow, with most new impervious covers concentrated in the northern parts. After 2010, the policy of "new urban area construction" was put into practice, incurring the emergence of various new types of imperviousness, such as buildings, traffic pavements and industrial plants.

4.3. Continuous impervious surface dynamics during the study period

Figs. 14 and 15 show the continuous impervious surface dynamics in the spatial and temporal domain, respectively. In Fig. 14, blue tones in the modeled pixels are assigned to early impervious surface expansion while yellow and red tones indicate later emergence of imperviousness. The gray color within the study area indicates the original impervious extent in the year 2002. The early wave of urban construction boom before 2005 was commonly observed in the adjacent areas of existing settlements, and most of them were in relatively small sizes. An exception is in the eastern part of Nanchang County, which was designated as a university town by the local government prior to 2000. In effect, impervious surfaces in this region expanded earlier. After 2013, the study area experienced another period of rapid impervious expansion, with most of the increase occurring in the southern parts, especially Xinjian District and Nanchang County.

Fig. 15 shows the temporal trajectory of impervious surface expansion in Nanchang. Overall, the original and error-adjusted area estimations are similar throughout the entire study period. Temporally, we observe accelerated expansion rates of impervious surface, with relatively high rates before 2005 and after 2012. The rates are in accordance with the annual nighttime light dynamic time series, reflecting actual infrastructure construction activities in Nanchang. At the quarterly scale, the analysis also captures intra-annual variations where the second half of the year has more impervious surface expansion areas than the first half, which reflects the construction activities in reality (Zhang et al., 2017).

4.4. Comparison with other existing products

Table 4 provides the statistics of impervious surface areas using our error-adjusted estimations and other five existing products. It should be noted that none of these reference products can be considered as ground truth. Alternatively, the inter-comparison offers an insight of agreement level between our data outputs and other products in the study area. Overall, there are considerable variations among the
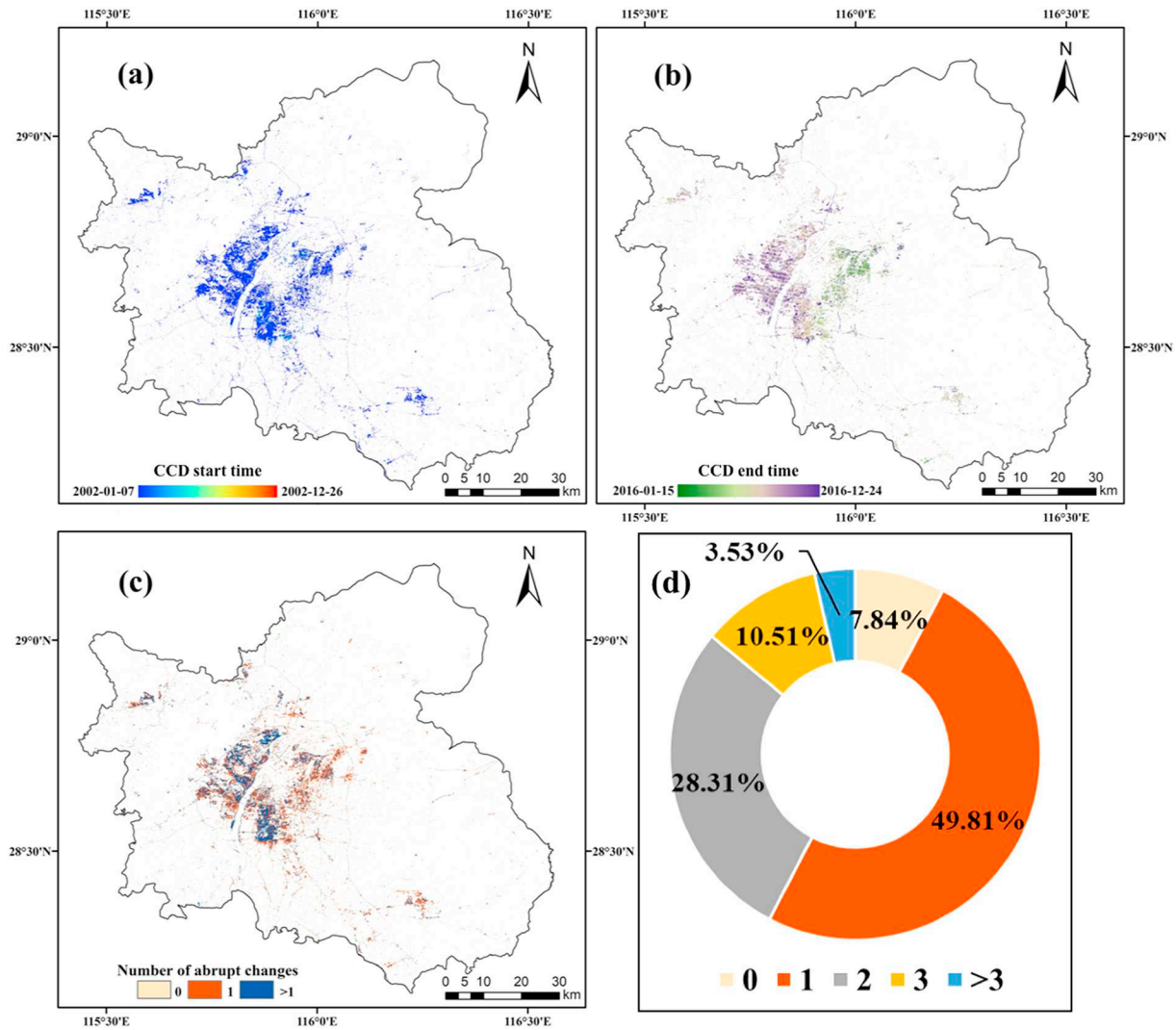
Fig. 9. Key outputs from CCD for change detection. (a) CCD start date, (b) CCD end date, (c) number of abrupt changes, (d) percentages of different abrupt change numbers.
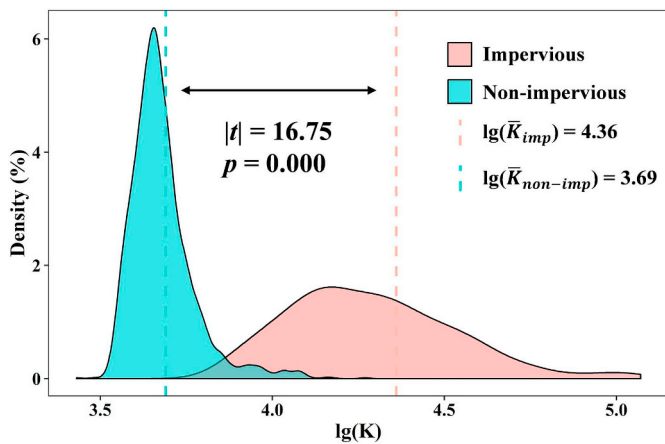

Fig. 10. Relative frequency of the index K (in the logarithmic form). $\overline{K}_{imp}$ and $\overline{K}_{non}$ indicate the mean values of impervious and non-impervious covers. Adjusted *t*-test (for unequal variance) is used to test the difference in means.

different datasets, and our outputs are in the medium level. Moreover, all products, except for GHS, reveal a consistent increase across the available epochs, reflecting a general trend of impervious surface expansion in Nanchang. An interesting finding is that the total impervious

surface areas of the three pixel-based estimates (GHS, FROM-GLC and our outputs) are constantly smaller than those of the other three products. For example, in 2010 when most products were available, only CAS-NLCD, NUACI and GLC30 reached 450 km^2. The greatest discrepancy occurred in 2005 when the total impervious surface areas of CAS-NLCD and NUACI nearly doubled our estimate. Although only one year (2014) can be compared, GHS is found to have a similar estimate to this study, with impervious surface areas of 514.04 km^2 and 485.73 ± 4.43 km^2, respectively. FROM-GLC, on the contrary, constantly displays the lowest estimate in the available years (i.e., 2010 and 2015).

Fig. 16 shows the comparison of impervious surface maps in the study area in 2010. Compared to the false color composite Landsat image, footprints from all estimates reasonably agree with each other, although differences are substantial in some areas. Specifically, there is a good agreement in highly urbanized regions, but CAS-NLCD and NUACI generally estimate larger patch sizes than other datasets. In addition, only GLC30, FROM-GLC and our outputs capture the spatial pattern of highway network to some degree. The greatest differences in magnitude are found in rural regions where the two pixel-based predictions (this study and FROM-GLC) yield greater numbers of small-scale impervious surface clusters.

Fig. 17 further compares different datasets for the year of 2010 by selecting three 18 × 18 km regions, each of which represents one
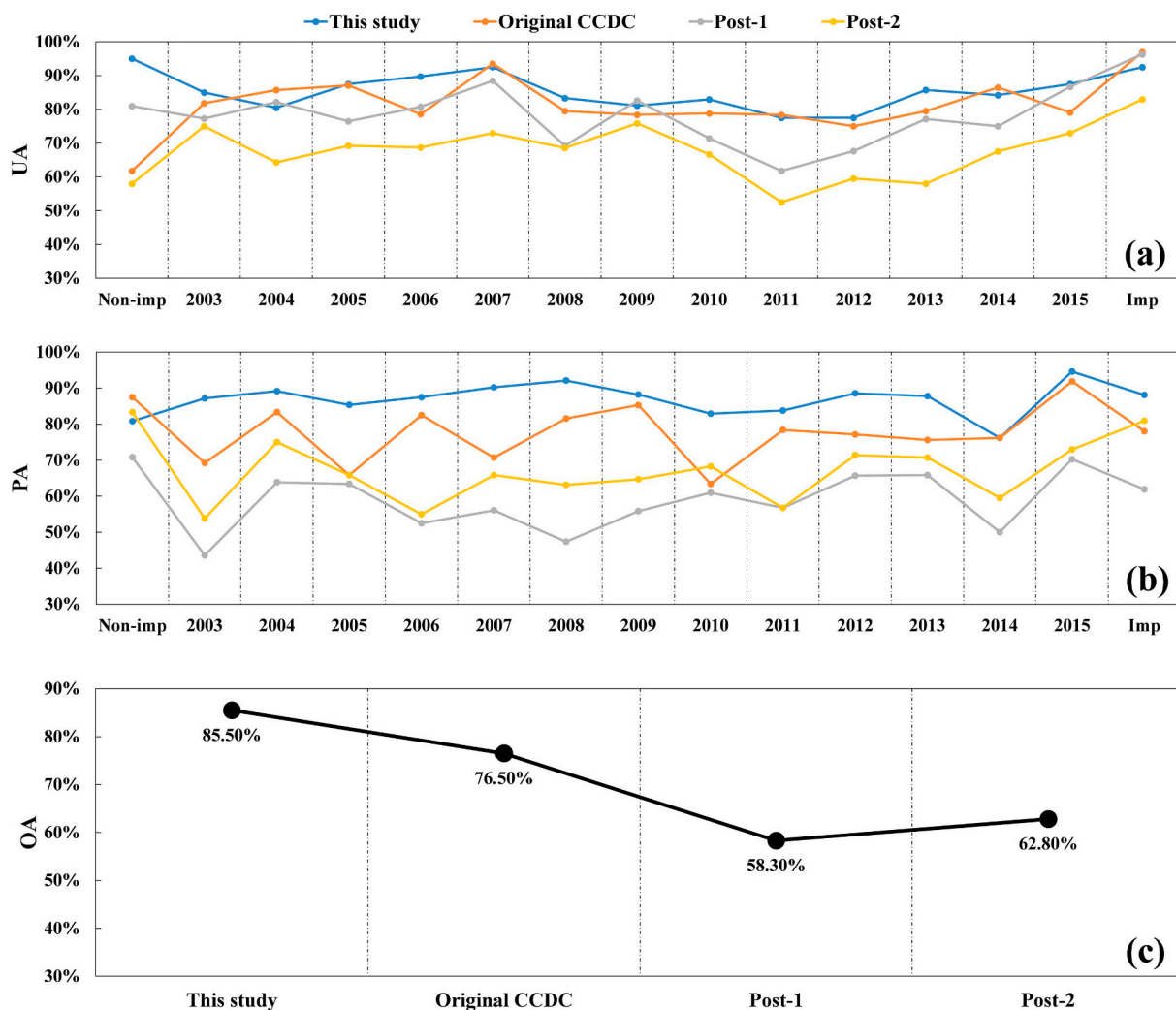
Fig. 11. Performances of annual-scale impervious surface change detection using different approaches based on the 15 classes described in Table 1. (a) User's accuracy, (b) producer's accuracy, and (c) overall accuracy. Post-1 and Post-2 represent post-classification approaches without and with temporal consistency check, respectively.

typical landscape. All the products show similar patterns in the urban core region where nearly half of the areas are covered by impervious surfaces. These datasets correctly capture most impervious surface areas except those in the islands located within Ganjiang river (upper middle the urban core subset). Compared to other datasets, FROM-GLC and our outputs exhibit weaker imperviousness in the eastern and southern parts of Nanchang. In the sub-urban region, major impervious clusters are detected by all estimates, but their patterns substantially vary. In NUACI, almost all impervious clusters are connected, leaving the remaining areas identified as natural lands. This highly concentrated distribution, however, is not observed in other products. Again, the impervious surface extent in FROM-GLC is similar to our estimate, especially in the southern parts dominated by sparse built-ups and traffic pavements. However, FROM-GLC is not able to detect settlements in the northwestern corner and some parts of Changbei International Airport in the center, both of which are identified by our outputs, GLC30 and CAS-NLCD. In the countryside region, the overall picture of the impervious surface distribution is quite heterogeneous among the different datasets. Not surprisingly, the impervious surface extent of NUACI is still smaller than the other products. Our dataset is similar to FROM-GLC in terms of the overall impervious surface distribution and magnitude. GLC30 and CAS-NLCD, on the other hand, show greater imperviousness estimates than the other products.

5. Discussion

5.1. Spatial-temporal rules for continuous impervious surface dynamics

Tracking human-dominated or -induced land cover and land use dynamics is of critical importance to understanding the global processes (Kareiva et al., 2007; Prestele et al., 2016; Zhang et al., 2018b). Unlike the other land cover changes, the transition from natural lands to impervious cover follows certain spatial-temporal rules, which can facilitate change detection analysis. In this study, we incorporate these rules in extracting impervious surface dynamics and obtain comparably satisfactory results. Our approach offers a new perspective for tracking continuous impervious surface change in a timely and cost-effective manner.

In the spatial domain, the stable area masking procedure greatly improves computing efficiency. According to our results, < 5% of the study area has experienced impervious surface expansion during 2002–2016 (Table 3), meaning that over 95% of processing workload has been saved. Masking out irrelevant regions also effectively alleviates classification errors incurred by cloud cover, ETM+ SLC-off problem, and data missing (Deng et al., 2017). These errors could be propagated in post-classification approaches, reducing change detection accuracy.
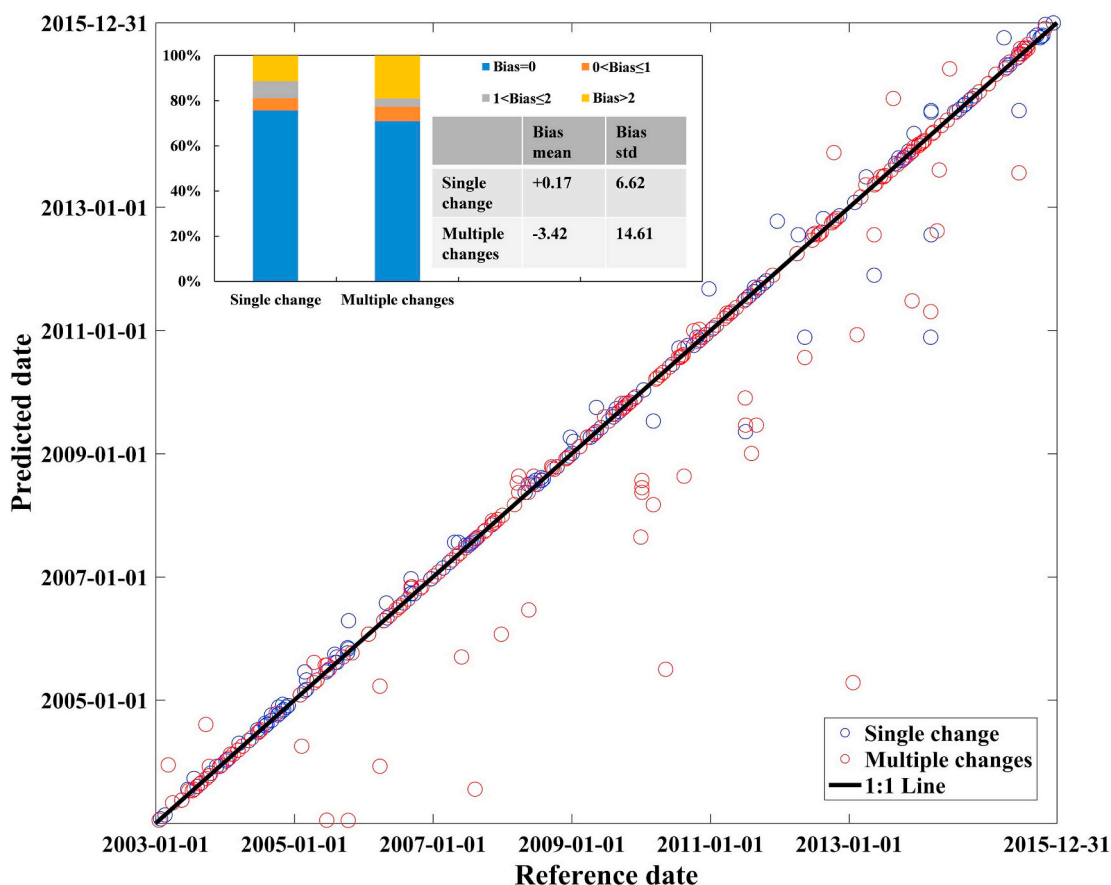
Fig. 12. Continuous-scale performance of impervious surface change detection. All temporal bias statistics are re-scaled in accordance to the temporal resolution of Landsat revisit period of 16 days.

In the temporal domain, the irreversibility of impervious surface expansion has been widely recognized and applied to refine impervious surface dynamic monitoring results (Gao et al., 2012; Schneider and Mertes, 2014; Shao and Liu, 2014). Most previous studies usually adopted temporal consistency check to correct unreasonable land cover changes (Li et al., 2015; Zhang and Weng, 2016; Zhang et al., 2017; Zhang et al., 2018c), which nevertheless inevitably introduces further estimate biases, as demonstrated by our results in Fig. 11a, b. Our approach directly leverages the rule of irreversibility so that the change detection analysis can focus only on finding the time point of change from non-impervious to impervious surface.

5.2. Continuous change detection using dense Landsat time series stacks

Landsat has a unique place in the pantheon of satellite-based global land observing systems because of its long data archive history, fine spatial resolution and open-access policy (Woodcock et al., 2008; Wulder et al., 2016; Wulder et al., 2019; Zhu et al., 2019a). These advantages have promoted the applications of automatic and robust algorithms, with which more frequent Landsat time series can be handled (Huang et al., 2010; Kennedy et al., 2010; Verbesselt et al., 2012; Zhu, 2017; Wulder et al., 2018). In this study, we adopt the CCD algorithm for impervious surface change detection using dense data stacks from Landsat 5, 7, and 8. This algorithm is found to be beneficial in revealing information that has been hindered by insufficient data frequency. For example, our study has observed intra-annual variations of impervious surface expansion (Fig. 15).

In the present study, we integrate the irreversibility of impervious surface expansion into the CCD algorithm. First, CCD detects persistent pixels misclassified in the spatial masking procedure, and thus corrects

classification errors to some extent (Fig. 5b). Second, for pixels with multiple changes, we improve CCD by using the false alarm exclusion procedure, which efficiently captures the time point of imperviousness emergence. This integration shows the potential of generating more reliable change detection results than the original CCDC algorithm (Fig. 11).

5.3. Comparison with existing products

The derived impervious surface maps in this study are comparable to the reference datasets, most of which are estimated using more complex algorithms (e.g., GHS and NUACI) or involving manual intervention (e.g., CAS-NLCD). Our estimates share more spatial similarity with other datasets in highly urbanized regions than in peri-urban and rural areas where heterogeneous landscapes dominate, in accordance to Qin et al. (2017). Such a discrepancy can be due to the difference of the mapping algorithms and input data. GLC30 and CAS-NLCD are generated or partially assisted by visual interpretation, thus settlements in small sizes (e.g., villages) may be easily neglected. NUACI, on the other hand, is a rule-based product derived from Landsat imagery and DMSP-OLS nighttime lights. As a consequence, some impervious surfaces with low nightlight brightness could be incorrectly masked out (Zheng et al., 2017; Liu et al., 2018b). Within the urban core of Nanchang, river islands receive special attention because of the seasonality of inundations. Based on our knowledge, none of the five maps (Fig. 17) perfectly captures the ground truth of imperviousness in the river islands, indicating the impact of seasonal water occurrence on impervious surface mapping or change detection.

Another issue that may cause the difference is the inconsistency of the land cover classification scheme. For example, in GLC30, there is no
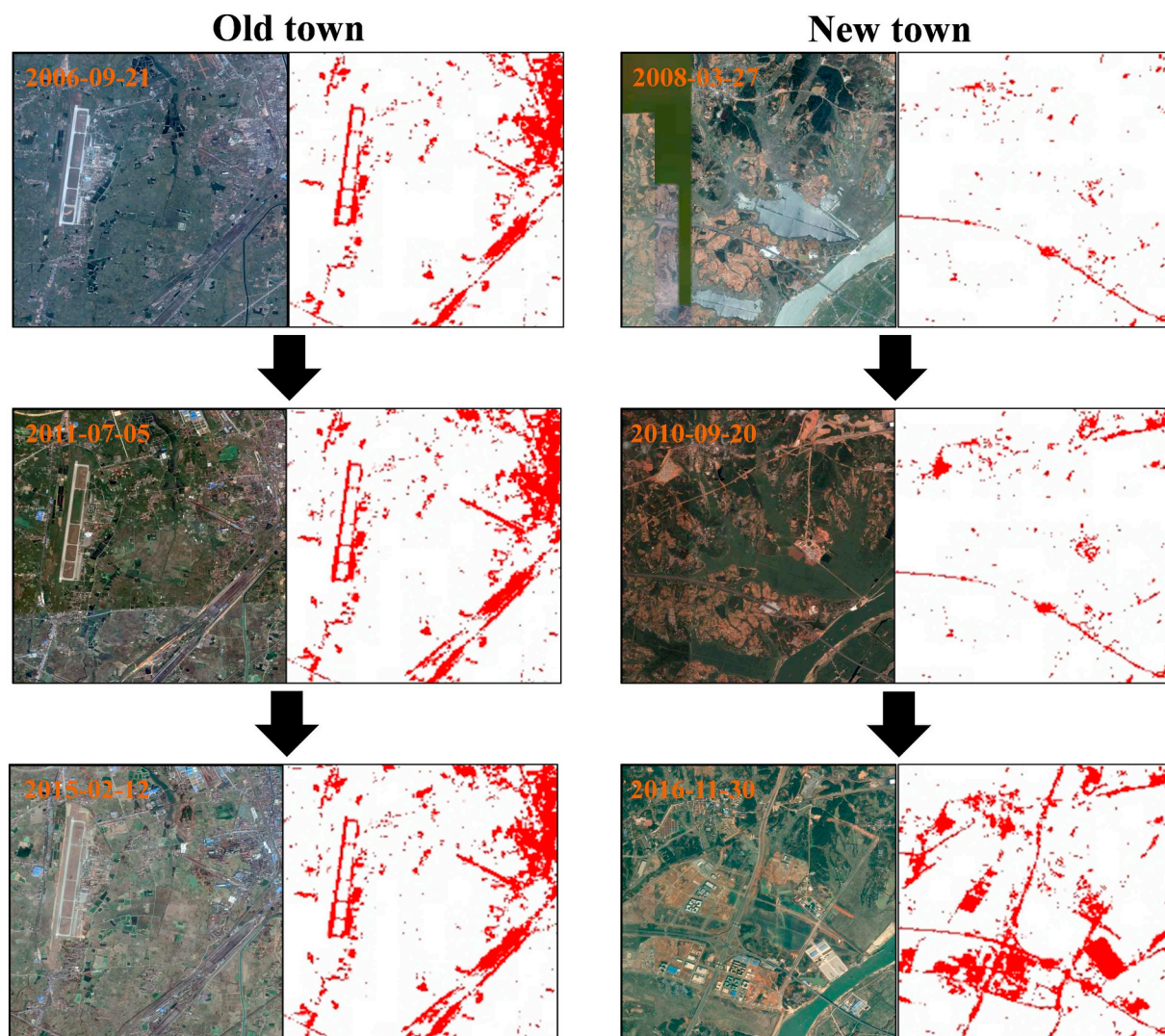
Old town

New town

Fig. 13. Illustration of comparing the generated impervious surface maps and corresponding Google Earth VHR images at given time points.

impervious surface class, thus we used the class of artificial surface as an alternative. This land cover type, however, contains non-impervious surfaces such as the urban green space (Chen et al., 2015). Therefore, a thorough evaluation of our mapping performance requires more established land cover products in which the class of impervious surface is included.

Due to the long temporal interval, current fine-resolution impervious surface (or analogous land cover type) products can capture some, but not all, of the imperviousness dynamics during urbanization. Our approach renders a new possibility to fill this gap. The independent classification of the two baseline years (see Section 3.1) can be replaced by the corresponding layers derived from existing datasets. Then, the stable area masking and continuous change detection can be implemented in sequence. The integration of existing products and our approach brings the following benefits. First, no additional data or manual intervention is required, so the product consistency can be met. More importantly, by generating more frequent impervious surface extent maps at the annual or even intra-annual scales, we are able to provide more nuanced insights for monitoring impervious surface dynamics that are not represented by estimates of existing products.

5.4. Uncertainties and limitations

Although accuracy assessments show good performance of the

present approach, our approach has limitations and uncertainties. The classification errors of the start and end years can induce uncertainties in the stable area mask. In this study, reference samples for modeling and validation are not strictly ground truth data, but rather extracted from satellite images via manual interpretation. This process contains errors, which may be propagated into the final outputs (Foody et al., 2016). The CCD algorithm depends heavily on high frequency of clear observations. Hence, its application may be limited in places with unfavorable weather conditions or extreme seasonal imbalance of clear observations. Since a "change target" method focuses only on impervious surfaces, the present approach cannot reveal the cause of change (i.e., change agent), which is equally important in understanding urban system dynamics (Kennedy et al., 2015). The heterogeneous nature of urban landscapes gives rise to the common presence of mixed pixels that can lead to a decreased change detection accuracy due to the spectral signature interference from other land cover types. Therefore, further studies may focus on sub-pixel level implementation of monitoring continuous impervious surface dynamics.

6. Conclusions

Accurately monitoring impervious surface dynamics is of great importance far beyond the city limit. In this study, we develop an approach for continuous impervious surface change estimation with the
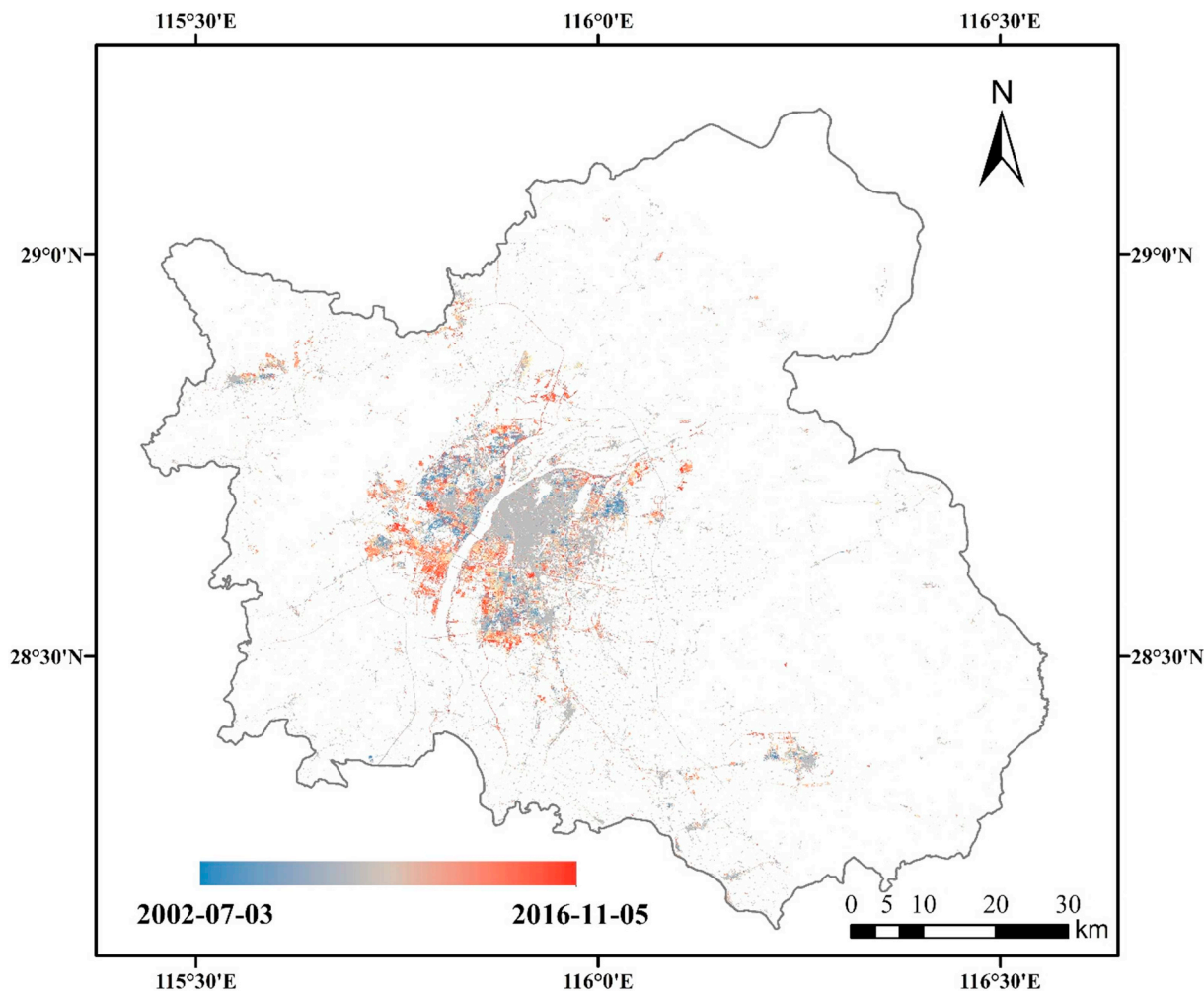
Fig. 14. Spatial distribution of the dates of impervious surface emergence. The gray color represents the impervious surface extent at the initial stage (the year of 2002).

use of the spatial-temporal rules and dense time series stacks of Landsat data. Experimental results in Nanchang, China, reveal the effectiveness and efficiency of this approach. Three major conclusions are summarized. First, by applying classification in the start and end years, stable areas characterized by temporally persistent land covers or irrelevant land cover changes can be spatially excluded, saving unnecessary computing workload. Second, based on the temporal irreversibility rule and the CCD algorithm, continuous change detection can be achieved on the per-pixel level by finding the corresponding breaks (i.e., change time points) through time series models using Landsat dense time
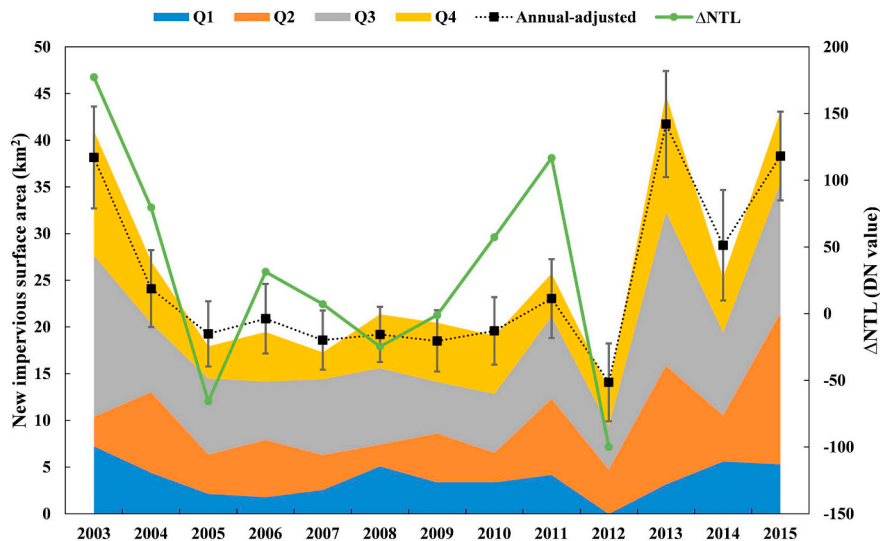

Fig. 15. Temporal trajectory of new impervious surface areas. The dotted line represents error-adjusted impervious surface expansion areas with uncertainties (95% confidence interval) at the annual scale. Q1, Q2, Q3 and Q4 represent the periods of January–March, April–June, July–September, and October–December, respectively. ΔNTL denotes the difference of nighttime light between one given year and its previous year.

Table 4
Comparison of impervious surface areas among different products (unit in km²).

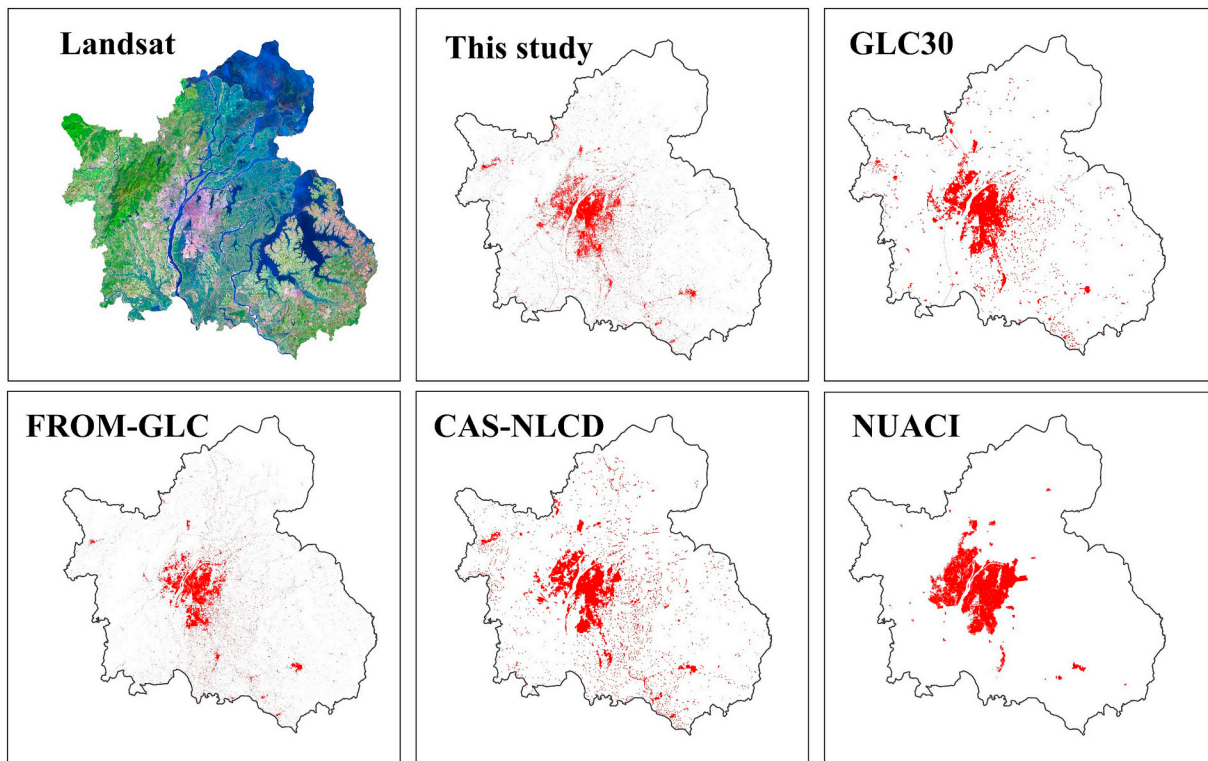| Year	GLC30	GHS	CAS-NLCD	FROM-GLC	NUACI	This study
2005			517.19		517.87	276.83 ± 5.30
2010	473.38		537.62	334.43	571.44	375.31 ± 5.72
2014		514.04				485.73 ± 4.43
2015			621.26	524.62		524.89 ± 3.93

Fig. 16. Spatial comparison of impervious surface maps in 2010. SWIR2, NIR, and RED are displayed in as red, green and blue layers for the Landsat image. (For interpretation of the references to color in this figure legend, the reader is referred to the web version of this article.)
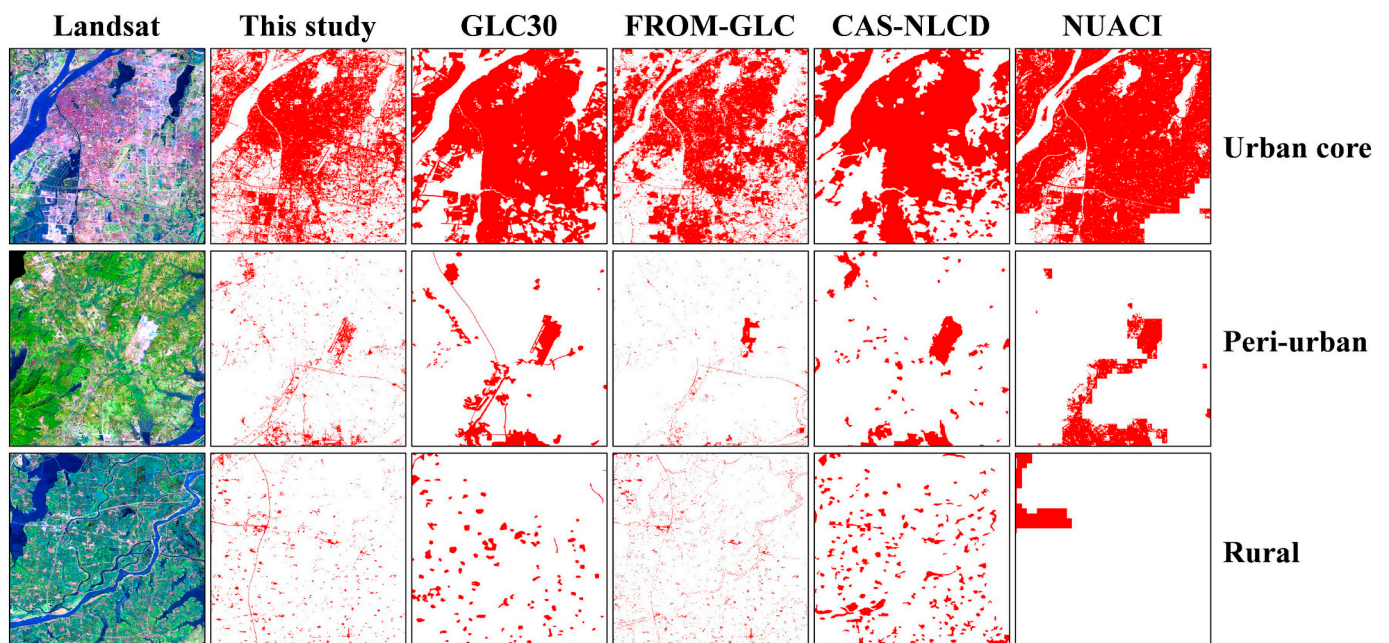

Fig. 17. Impervious surface mapping results of three typical regions in 2010. SWIR2, NIR, and RED are displayed in as red, green and blue layers for the Landsat image. (For interpretation of the references to color in this figure legend, the reader is referred to the web version of this article.)

series. Thus, an impervious surface extent map at any given time during the study period can be generated. Finally, compared to the traditional impervious surface change monitoring methods, the present approach not only provides convincing and more frequent estimates, but also has the flexibility to be integrated into the existing products for further utilization at the varying spatial and temporal scales.

Acknowledgements

Appendix A

A.1. Post-classification without temporal consistency check (Post-1 approach)

We implemented the Post-1 approach through directly performing annual classifications from 2002 to 2016. For the years 2002 and 2016, we directly used our classification results. For the remaining years, the same methodology provided in Sections 3.1.1 and 3.1.2 (including seasonal image compositing, feature extraction, land cover class scheme and classifier parameterization) was used to generate their classification results. Considering the classification consistence in different years, we adopted a "backdating" procedure (Xu et al., 2018) for multi-year training sample collection. We treated the training sample set of 2016 as the baseline due to the availability of adequate VHR imagery. Then, we checked these samples in the previous year (i.e., 2015) to identify whether the land cover types have changed. For samples with changed land cover, we re-assigned their class labels in that year. This step was repeated until 2003. To ensure the reliability, we removed the samples that were difficult to interpret, resulting in different sample size for each year during 2002–2016 (Table A1). Note that the initial output of annual classification was a six-category (impervious surface, bareland, cropland, forest, wetland and water) land cover map. Thus, a re-classification procedure was conducted to re-group six land covers into impervious surface and non-impervious surface.

A.2. Post-classification with temporal consistency check (Post-2 approach)

Based on the annual classification results from Section A.1, the Post-2 approach utilized a temporal consistency check (Li et al., 2015) to improve impervious surface sequence consistency. Specifically, the temporal consistency check includes two steps, described as follows.

Step 1 is iteratively temporal filtering. Given original annual classification sequence $Y = \{Y_1, Y_2, ..., Y_n\}$, a temporal consistency probability for each year Y_i can be calculated as:

$$P_i = \frac{\sum_{j=i-r}^{i+r} Con(Y_i, Y_j)}{2r + 1} \tag{A.1}$$

where P_i is the temporal consistency probability, $Con()$ denotes a discriminant function returning 1 ($Y_i = Y_j$) or 0 ($Y_i \neq Y_j$), r is the length of temporal window, which was initially set to 1 (Li et al., 2015). Then we used the acquired temporal consistency probability sequence $P = \{P_2, ..., P_{n-1}\}$ to refine Y, written as:

$$Z_i = \begin{cases} Y_i, P_i \geq 0.5 \\ opposite, P_i < 0.5 \end{cases} \tag{A.2}$$

where Z_i is the refined annual classification result, *opposite* denotes the initial class label should be changed to its opposite, so Y (except the start and the end years) can be updated to $Z = \{Y_1, Z_2, ..., Z_{n-1}, Y_n\}$. The above procedure was conducted repeatedly with a gradually increasing r until P_i for all years are > 0.5.

Step 2 is logistic reasoning. While the temporal filtering can reduce spurious changes in the temporal domain, unreasonable results (i.e., those against the unidirectionally of impervious surface change) may still exist. In addition, the initial classification results within the start and end years cannot be updated by the iteratively temporal filtering due to the lack of temporal contexts. Therefore, a logistic reasoning was further implemented. First, a temporal segmentation was applied according to the final temporal window length, resulting in three periods named as Seg-head, Seg-body and Seg-tail, respectively. Then a temporal majority voting method was applied to Seg-body for identifying whether it is impervious surface dominated (i.e., impervious surface years are more than non-impervious years) or not. In the case of dominated impervious surface, we chose the first impervious year as the turning point. Otherwise, the turning point was identified as the last non-impervious year. We modified Seg-body as non-impervious prior to the turning point and as impervious surface after the turning point. Finally, based on the modified Seg-body, similar reasoning processes were applied to the whole sequence.

A.3. The original CCDC algorithm

We implemented the original CCDC algorithm using the Python codes provided by the U.S. Geological Survey (https://github.com/USGS-EROS/lcmap-pyclass). The time series model coefficients and Root Mean Square Errors (RMSE) from all seven Landsat bands (green, blue, red, NIR, SWIR1, SWIR2 and thermal) were used as input features for classification (Zhu et al., 2015). We used the training samples acquired in 2002 and 2016 to parameterize the RFC and predict land cover classes. Since the classification result generated from original CCDC is continuous, we selected the same fixed date of the year as that in the main text (December 31st) to produce the annual classification sequence.

Table A1

Training sample sizes for the two post-classification approaches during 2002–2016.

Class	Bareland	Cropland	Forest	Impervious	Water	Wetland	Total
2002	64	1527	832	220	151	137	2931
2003	61	1525	832	227	137	136	2918
2004	70	1523	832	243	136	136	2940
2005	68	1520	832	274	136	136	2966
2006	67	1515	829	283	136	136	2966
2007	79	1513	829	285	136	136	2978
2008	87	1511	829	307	136	136	3006
2009	84	1510	829	323	136	136	3018
2010	82	1507	829	327	136	136	3017
2011	84	1507	829	335	136	136	3027
2012	93	1509	832	334	136	136	3040
2013	88	1509	832	342	136	136	3043
2014	88	1508	874	351	136	136	3093
2015	86	1500	879	350	136	136	3087
2016	87	1497	837	340	222	136	3119

References

Arnold Jr., C.L., Gibbons, C.J., 1996. Impervious surface coverage: the emergence of a key environmental indicator. J. Am. Plan. Assoc. 62 (2), 243–258. https://doi.org/10.1080/01944369608975688.

Bagan, H., Yamagata, Y., 2012. Landsat analysis of urban growth: how Tokyo became the world's largest megacity during the last 40 years. Remote Sens. Environ. 127, 210–222. https://doi.org/10.1016/j.rse.2012.09.011.

Batty, M., 2011. When all the world's a city. Environ Plan A 43 (4), 765–772. https://doi.org/10.1068/a43403.

Boggs, J.L., Sun, G., 2011. Urbanization alters watershed hydrology in the Piedmont of North Carolina. Ecohydrology 4 (2), 256–264. https://doi.org/10.1002/eco.198.

Brun, S.E., Band, L.E., 2000. Simulating runoff behavior in an urbanizing watershed. Comput. Environ. Urban. Syst. 24 (1), 5–22. https://doi.org/10.1016/S0198-9715(99)00040-X.

Chen, Y., Li, X., Liu, X., Ai, B., 2014. Modeling urban land-use dynamics in a fast developing city using the modified logistic cellular automaton with a patch-based simulation strategy. Int. J. Geogr. Inf. Sci. 28 (2), 234–255. https://doi.org/10.1080/13658816.2013.831868.

Chen, J., Chen, J., Liao, A., Cao, X., Chen, L., Chen, X., He, C., Han, G., Peng, S., Lu, M., Zhang, W., Tong, X., Mills, J., 2015. Global land cover mapping at 30 m resolution: a POK-based operational approach. ISPRS J. Photogramm. Remote Sens. 103, 7–27. https://doi.org/10.1016/j.isprsjprs.2014.09.002.

Dannenberg, M.P., Hakkenberg, C.R., Song, C., 2016. Consistent classification of Landsat time series with an improved automatic adaptive signature generalization algorithm. Remote Sens. 8 (8), 691. https://doi.org/10.3390/rs8080691.

Deng, C., Wu, C., 2013. Examining the impacts of urban biophysical compositions on surface urban heat island: a spectral unmixing and thermal mixing approach. Remote Sens. Environ. 131, 262–274. https://doi.org/10.1016/j.rse.2012.12.020.

Deng, C., Zhu, Z., 2018. Continuous subpixel monitoring of urban impervious surface using Landsat time series. Remote Sens. Environ. https://doi.org/10.1016/j.rse.2018.10.011. In press.

Deng, C., Li, C., Zhu, Z., Lin, W., Xi, L., 2017. Subpixel urban impervious surface mapping: the impact of input Landsat images. ISPRS J. Photogramm. Remote Sens. 133, 89–103. https://doi.org/10.1016/j.isprsjprs.2017.09.015.

Foody, G.M., Pal, M., Rocchini, D., Garzon-Lopez, C.X., Bastin, L., 2016. The sensitivity of mapping methods to reference data quality: training supervised image classifications with imperfect reference data. ISPRS International Journal of Geo-Information 5 (11), 199. https://doi.org/10.3390/ijgi5110199.

Gao, F., Eric, B.D.C., Ma, R., Weng, Q., Masek, J.G., Chen, J., Yao, Pan, Song, C., 2012. Mapping impervious surface expansion using medium-resolution satellite image time series: a case study in the Yangtze River Delta, China. Int. J. Remote Sens. 33 (24), 7609–7628. https://doi.org/10.1080/01431161.2012.700424.

Gong, P., Liang, S., Carlton, E.J., Jiang, Q., Wu, J., Wang, L., Remais, J.V., 2012. Urbanisation and health in China. Lancet 379 (9818), 843–852. https://doi.org/10.1016/S0140-6736(11)61878-3.

Gong, P., Wang, J., Yu, L., Zhao, Y., Zhao, Y., Liang, L., Niu, Z., Huang, X., Fu, H., Liu, S., Li, C., Li, X., Fu, W., Liu, C., Xu, Y., Wang, X., Cheng, Q., Hu, L., Yao, W., Zhang, H., Zhu, P., Zhao, Z., Zhang, H., Zheng, Y., Ji, L., Zhang, Y., Chen, H., Yan, A., Guo, J., Yu, L., Wang, L., Liu, X., Shi, T., Zhu, M., Chen, Y., Yang, G., Tang, P., Xu, B., Giri, C., Clinton, N., Zhu, Z., Chen, J., Chen, J., 2013. Finer resolution observation and monitoring of global land cover: first mapping results with Landsat TM and ETM+ data. Int. J. Remote Sens. 34 (7), 2607–2654. https://doi.org/10.1080/01431161.2012.748992.

Gong, P., Yu, L., Li, C., Wang, J., Liang, L., Li, X., Ji, L., Bai, Y., Cheng, Y., Zhu, Z., 2016. A new research paradigm for global land cover mapping. Ann. GIS 22 (2), 87–102. https://doi.org/10.1080/19475683.2016.1164247.

Gorelick, N., Hancher, M., Dixon, M., Ilyushchenko, S., Thau, D., Moore, R., 2017. Google earth engine: planetary-scale geospatial analysis for everyone. Remote Sens. Environ. 202, 18–27. https://doi.org/10.1016/j.rse.2017.06.031.

Grimm, N.B., Faeth, S.H., Golubiewski, N.E., Redman, C.L., Wu, J., Bai, X., Briggs, J.M., 2008. Global change and the ecology of cities. Science 319 (5864), 756–760. https://doi.org/10.1126/science.1150195.

Hao, L., Sun, G., Liu, Y., Wan, J., Qin, M., Qian, H., Liu, C., Zheng, J., John, R., Fan, P., Chen, J., 2015. Urbanization dramatically altered the water balances of a paddy field dominated basin in southern China. Hydrol. Earth Syst. Sci. 12, 1941–1972. https://doi.org/10.5194/hess-19-3319-2015.

Huang, C., Goward, S.N., Masek, J.G., Thomas, N., Zhu, Z., Vogelmann, J.E., 2010. An automated approach for reconstructing recent forest disturbance history using dense Landsat time series stacks. Remote Sens. Environ. 114 (1), 183–198. https://doi.org/10.1016/j.rse.2009.08.017.

Hurd, J.D., Civco, D.L., 2004. Temporal characterization of impervious surfaces for the state of Connecticut. In: ASPRS Annual Conference Proceedings, Denver, Colorado.

Kareiva, P., Watts, S., McDonald, R., Boucher, T., 2007. Domesticated nature: shaping landscapes and ecosystems for human welfare. Science 316 (5833), 1866–1869. https://doi.org/10.1126/science.1140170.

Kennedy, R.E., Yang, Z., Cohen, W.B., 2010. Detecting trends in forest disturbance and recovery using yearly Landsat time series: 1. LandTrendr—temporal segmentation algorithms. Remote Sens. Environ. 114 (12), 2897–2910. https://doi.org/10.1016/j.rse.2010.07.008.

Kennedy, R.E., Yang, Z., Braaten, J., Copass, C., Antonova, N., Jordan, C., Nelson, P., 2015. Attribution of disturbance change agent from Landsat time-series in support of habitat monitoring in the Puget Sound region, USA. Remote Sens. Environ. 166, 271–285. https://doi.org/10.1016/j.rse.2015.05.005.

Li, X., Gong, P., 2016. An "exclusion-inclusion" framework for extracting human settlements in rapidly developing regions of China from Landsat images. Remote Sens. Environ. 186, 286–296. https://doi.org/10.1016/j.rse.2016.08.029.

Li, X., Gong, P., Liang, L., 2015. A 30-year (1984–2013) record of annual urban dynamics of Beijing City derived from Landsat data. Remote Sens. Environ. 166, 78–90. https://doi.org/10.1016/j.rse.2015.06.007.

Li, X., Zhou, Y., Zhu, Z., Liang, L., Yu, B., Cao, W., 2018. Mapping annual urban dynamics (1985–2015) using time series of Landsat data. Remote Sens. Environ. 216, 674–683. https://doi.org/10.1016/j.rse.2018.07.030.

Liu, C., Luo, H., Yao, Y., 2017. Optimizing subpixel impervious surface area mapping through adaptive integration of spectral, phenological, and spatial features. IEEE Geosci. Remote Sens. Lett. 14 (7), 1017–1021. https://doi.org/10.1109/LGRS.2017.2692799.

Liu, C., Xiong, T., Gong, P., Qi, S., 2018a. Improving large-scale moso bamboo mapping based on dense Landsat time series and auxiliary data: a case study in Fujian Province, China. Remote Sens. Lett. 9 (1), 1–10. https://doi.org/10.1080/2150704X.2017.1378454.

Liu, X., Hu, G., Chen, Y., Li, X., Xu, X., Li, S., Pei, F., Wang, S., 2018b. High-resolution multi-temporal mapping of global urban land using Landsat images based on the Google Earth Engine Platform. Remote Sens. Environ. 209, 227–239. https://doi.org/10.1016/j.rse.2018.02.055.

Mertes, C.M., Schneider, A., Sulla-Menashe, D., Tatem, A.J., Tan, B., 2015. Detecting change in urban areas at continental scales with MODIS data. Remote Sens. Environ. 158, 331–347. https://doi.org/10.1016/j.rse.2014.09.023.

Olofsson, P., Foody, G.M., Stehman, S.V., Woodcock, C.E., 2013. Making better use of accuracy data in land change studies: estimating accuracy and area and quantifying uncertainty using stratified estimation. Remote Sens. Environ. 129, 122–131. https://doi.org/10.1016/j.rse.2012.10.031.

Olofsson, P., Holden, C.E., Bullock, E.L., Woodcock, C.E., 2016. Time series analysis of satellite data reveals continuous deforestation of New England since the 1980s. Environ. Res. Lett. 11 (6), 064002. https://doi.org/10.1088/1748-9326/11/6/064002.

Pal, M., 2005. Random forest classifier for remote sensing classification. Int. J. Remote Sens. 26 (1), 217–222. https://doi.org/10.1080/01431160412331269698.

Pengra, B., Gallant, A.L., Zhu, Z., Dahal, D., 2016. Evaluation of the initial thematic output from a continuous change-detection algorithm for use in automated operational land-change mapping by the US Geological Survey. Remote Sens. 8 (10), 811.

https://doi.org/10.3390/rs8100811.

Pesaresi, M., Ehrlich, D., Ferri, S., Florczyk, A., Carneiro, F.S., Halkia, S., Julea, A., Kemper, T., Soille, P., Syrris, V., 2016. Operating Procedure for the Production of the Global Human Settlement Layer from Landsat Data of the Epochs 1975, 1990, 2000, and 2014. Technical Report EUR 27741 EN. Publications Office of the European Union, Joint Research Centre of the European Commission.

Prestele, R., Alexander, P., Rounsevell, M.D., Arneth, A., Calvin, K., Doelman, J., Eitelberg, D.A., Engström, K., Fujimori, S., Hasegawa, T., Havlik, P., Humpenöder, F., Jain, A.K., Krisztin, T., Kyle, P., Meiyappan, P., Popp, A., Sands, R.D., Schaldach, R., Schüngel, J., Tabeau, A., Van Meijl, H., Van Vliet, J., Verburg, P.H., 2016. Hotspots of uncertainty in land-use and land-cover change projections: a global-scale model comparison. Glob. Chang. Biol. 22 (12), 3967–3983. https://doi.org/10.1111/gcb.13337.

Qin, Y., Xiao, X., Dong, J., Chen, B., Liu, F., Zhang, G., Zhang, Y., Wang, J., Wu, X., 2017. Quantifying annual changes in built-up area in complex urban-rural landscapes from analyses of PALSAR and Landsat images. ISPRS J. Photogramm. Remote Sens. 124, 89–105. https://doi.org/10.1016/j.isprsjprs.2016.12.011.

Schneider, A., 2012. Monitoring land cover change in urban and peri-urban areas using dense time stacks of Landsat satellite data and a data mining approach. Remote Sens. Environ. 124, 689–704. https://doi.org/10.1016/j.rse.2012.06.006.

Schneider, A., Mertes, C.M., 2014. Expansion and growth in Chinese cities, 1978–2010. Environ. Res. Lett. 9 (2), 024008. https://doi.org/10.1088/1748-9326/9/2/024008.

Schneider, A., Friedl, M.A., Potere, D., 2010. Mapping global urban areas using MODIS 500-m data: new methods and datasets based on 'urban ecoregions'. Remote Sens. Environ. 114 (8), 1733–1746. https://doi.org/10.1016/j.rse.2010.03.003.

Seto, K.C., Woodcock, C.E., Song, C., Huang, X., Lu, J., Kaufmann, R.K., 2002. Monitoring land-use change in the Pearl River Delta using Landsat TM. Int. J. Remote Sens. 23 (10), 1985–2004. https://doi.org/10.1080/01431160110075532.

Seto, K.C., Fragkias, M., Güneralp, B., Reilly, M.K., 2011. A meta-analysis of global urban land expansion. PLoS One 6 (8), e23777. https://doi.org/10.1371/journal.pone.0023777.

Seto, K.C., Güneralp, B., Hutyra, L.R., 2012. Global forecasts of urban expansion to 2030 and direct impacts on biodiversity and carbon pools. Proc. Natl. Acad. Sci. U. S. A. 109 (40), 16083–16088. https://doi.org/10.1073/pnas.1211658109.

Sexton, J.O., Song, X.P., Huang, C., Channan, S., Baker, M.E., Townshend, J.R., 2013. Urban growth of the Washington, DC–Baltimore, MD metropolitan region from 1984 to 2010 by annual, Landsat-based estimates of impervious cover. Remote Sens. Environ. 129, 42–53. https://doi.org/10.1016/j.rse.2012.10.025.

Shao, Z., Liu, C., 2014. The integrated use of DMSP-OLS nighttime light and MODIS data for monitoring large-scale impervious surface dynamics: a case study in the Yangtze River Delta. Remote Sens. 6 (10), 9359–9378. https://doi.org/10.3390/rs6109359.

Singh, A., 1989. Review article digital change detection techniques using remotely-sensed data. Int. J. Remote Sens. 10 (6), 989–1003. https://doi.org/10.1080/01431168908903939.

Song, X.P., Sexton, J.O., Huang, C., Channan, S., Townshend, J.R., 2016. Characterizing the magnitude, timing and duration of urban growth from time series of Landsat-based estimates of impervious cover. Remote Sens. Environ. 175, 1–13. https://doi.org/10.1016/j.rse.2015.12.027.

Tucker, C.J., 1979. Red and photographic infrared linear combinations for monitoring vegetation. Remote Sens. Environ. 8 (2), 127–150. https://doi.org/10.1016/0034-4257(79)90013-0.

United Nations (UN), 2014. World Urbanization Prospects: The 2014 Version-Highlights. Department of Economic and Social Affairs, New York.

Verbesselt, J., Zeileis, A., Herold, M., 2012. Near real-time disturbance detection using satellite image time series. Remote Sens. Environ. 123, 98–108. https://doi.org/10.1016/j.rse.2012.02.022.

Weng, Q., 2012. Remote sensing of impervious surfaces in the urban areas: requirements, methods, and trends. Remote Sens. Environ. 117, 34–49. https://doi.org/10.1016/j.rse.2011.02.030.

White, J.C., Wulder, M.A., Hobart, G.W., Luther, J.E., Hermosilla, T., Griffiths, P., Coops, N.C., Hall, R.J., Hostert, P., Dyk, A., Guindon, L., 2014. Pixel-based image compositing for large-area dense time series applications and science. Can. J. Remote. Sens. 40 (3), 192–212. https://doi.org/10.1080/07038992.2014.945827.

Woodcock, C.E., Allen, R., Anderson, M., Belward, A., Bindschadler, R., Cohen, W., Gao, F., Goward, S.N., Helder, D., Helmer, E., Nemani, R., Oreopoulos, L., Schott, J., Thenkabail, P.S., Vermote, E.F., Vogelmann, J., Wulder, M.A., Wynne, R., 2008. Free access to Landsat imagery. Science 320 (5879), 1011. https://doi.org/10.1126/science.320.5879.1011a.

Wu, C., Du, B., Cui, X., Zhang, L., 2017. A post-classification change detection method based on iterative slow feature analysis and Bayesian soft fusion. Remote Sens. Environ. 199, 241–255. https://doi.org/10.1016/j.rse.2017.07.009.

Wulder, M.A., White, J.C., Loveland, T.R., Woodcock, C.E., Belward, A.S., Cohen, W.B., Fosnight, E.A., Shaw, J., Masek, J.G., Roy, D.P., 2016. The global Landsat archive: status, consolidation, and direction. Remote Sens. Environ. 185, 271–283. https://doi.org/10.1016/j.rse.2015.11.032.

Wulder, M.A., Coops, N.C., Roy, D.P., White, J.C., Hermosilla, T., 2018. Land cover 2.0. Int. J. Remote Sens. 39 (12), 4254–4284. https://doi.org/10.1080/01431161.2018.1452075.

Wulder, M.A., Loveland, T.R., Roy, D.P., Crawford, C.J., Masek, J.G., Woodcock, C.E., Allen, R.G., Anderson, M.C., Belward, A.S., Cohen, W.B., Dwyer, J., Erb, A., Gao, F., Griffiths, P., Helder, D., Hermosilla, T., Hipple, J.D., Hostert, P., Hughes, M.J., Huntington, J., Johnson, D.M., Kennedy, R., Kilic, A., Li, Z., Lymburner, L., McCorkel, J., Pahlevan, N., Scambos, T.A., Schaaf, C., Schott, J.R., Sheng, Y., Storey, J., Vermote, E., Vogelmann, J., White, J.C., Wynne, R.H., Zhu, Z., 2019. Current status of Landsat program, science, and applications. Remote Sens. Environ. 225, 127–147.

https://doi.org/10.1016/j.rse.2019.02.015.

Xian, G., Homer, C., 2010. Updating the 2001 National Land Cover Database impervious surface products to 2006 using Landsat imagery change detection methods. Remote Sens. Environ. 114 (8), 1676–1686. https://doi.org/10.1016/j.rse.2010.02.018.

Xu, H., 2006. Modification of normalised difference water index (NDWI) to enhance open water features in remotely sensed imagery. Int. J. Remote Sens. 27 (14), 3025–3033. https://doi.org/10.1080/01431160600589179.

Xu, H., Qi, S., Gong, P., Liu, C., Wang, J., 2018. Long-term monitoring of citrus orchard dynamics using time-series Landsat data: a case study in southern China. Int. J. Remote Sens. 39 (22), 8271–8292.

Yu, L., Wang, J., Li, X., Li, C., Zhao, Y., Gong, P., 2014. A multi-resolution global land cover dataset through multisource data aggregation. Sci. China Earth Sci. 57 (10), 2317–2329. https://doi.org/10.1007/s11430-014-4919-z.

Yu, W., Zhou, W., Qian, Y., Yan, J., 2016. A new approach for land cover classification and change analysis: integrating backdating and an object-based method. Remote Sens. Environ. 177, 37–47. https://doi.org/10.1016/j.rse.2016.02.030.

Yuan, F., Bauer, M.E., 2007. Comparison of impervious surface area and normalized difference vegetation index as indicators of surface urban heat island effects in Landsat imagery. Remote Sens. Environ. 106 (3), 375–386. https://doi.org/10.1016/j.rse.2006.09.003.

Zhang, L., Weng, Q., 2016. Annual dynamics of impervious surface in the Pearl River Delta, China, from 1988 to 2013, using time series Landsat imagery. ISPRS J. Photogramm. Remote Sens. 113, 86–96. https://doi.org/10.1016/j.isprsjprs.2016.01.003.

Zhang, Z., Wang, X., Zhao, X., Liu, B., Yi, L., Zuo, L., Wen, Q., Liu, F., Xu, J., Hu, S., 2014. A 2010 update of National Land use/cover database of China at 1:100000 scale using medium spatial resolution satellite images. Remote Sens. Environ. 149, 142–154. https://doi.org/10.1016/j.rse.2014.04.004.

Zhang, Q., Pandey, B., Seto, K.C., 2016. A robust method to generate a consistent time series from DMSP/OLS nighttime light data. IEEE Trans. Geosci. Remote Sens. 54 (10), 5821–5831. https://doi.org/10.1109/TGRS.2016.2572724.

Zhang, L., Weng, Q., Shao, Z., 2017. An evaluation of monthly impervious surface dynamics by fusing Landsat and MODIS time series in the Pearl River Delta, China, from 2000 to 2015. Remote Sens. Environ. 201, 99–114. https://doi.org/10.1016/j.rse.2017.08.036.

Zhang, Q., Hakkenberg, C.R., Song, C., 2018a. Evaluating the effectiveness of forest conservation policies with multi-temporal remotely sensed imagery: a case study from Tiantangzhai Township, Anhui, China. In: Liang, S. (Ed.), Comprehensive Remote Sensing. vol. 9. Elsevier, Oxford, pp. 39–58. https://doi.org/10.1016/B978-0-12-409548-9.10435-X.

Zhang, Q., Song, C., Chen, X., 2018b. Effects of China's payment for ecosystem services programs on cropland abandonment: a case study in Tiantangzhai Township, China. Land Use Policy 73, 239–248. https://doi.org/10.1016/j.landusepol.2018.01.001.

Zhang, L., Zhang, M., Yao, Y., 2018c. Mapping seasonal impervious surface dynamics in Wuhan urban agglomeration, China from 2000 to 2016. Int. J. Appl. Earth Obs. Geoinf. 70, 51–61. https://doi.org/10.1016/j.jag.2018.04.005.

Zheng, Q., Zeng, Y., Deng, J., Wang, K., Jiang, R., Ye, Z., 2017. "Ghost cities" identification using multi-source remote sensing datasets: a case study in Yangtze River Delta. Appl. Geogr. 80, 112–121. https://doi.org/10.1016/j.apgeog.2017.02.004.

Zhu, Z., 2017. Change detection using landsat time series: a review of frequencies, preprocessing, algorithms, and applications. ISPRS J. Photogramm. Remote Sens. 130, 370–384. https://doi.org/10.1016/j.isprsjprs.2017.06.013.

Zhu, Z., Woodcock, C.E., 2012. Object-based cloud and cloud shadow detection in Landsat imagery. Remote Sens. Environ. 118, 83–94. https://doi.org/10.1016/j.rse.2011.10.028.

Zhu, Z., Woodcock, C.E., 2014. Continuous change detection and classification of land cover using all available Landsat data. Remote Sens. Environ. 144, 152–171. https://doi.org/10.1016/j.rse.2014.01.011.

Zhu, Z., Woodcock, C.E., Rogan, J., Kellndorfer, J., 2012. Assessment of spectral, polarimetric, temporal, and spatial dimensions for urban and peri-urban land cover classification using Landsat and SAR data. Remote Sens. Environ. 117, 72–82. https://doi.org/10.1016/j.rse.2011.07.020.

Zhu, Z., Woodcock, C.E., Holden, C., Yang, Z., 2015. Generating synthetic Landsat images based on all available Landsat data: predicting Landsat surface reflectance at any given time. Remote Sens. Environ. 162, 67–83. https://doi.org/10.1016/j.rse.2015.02.009.

Zhu, Z., Fu, Y., Woodcock, C.E., Olofsson, P., Vogelmann, J.E., Holden, C., Wang, M., Dai, S., Yu, Y., 2016a. Including land cover change in analysis of greenness trends using all available Landsat 5, 7, and 8 images: a case study from Guangzhou, China (2000–2014). Remote Sens. Environ. 185, 243–257. https://doi.org/10.1016/j.rse.2016.03.036.

Zhu, Z., Gallant, A.L., Woodcock, C.E., Pengra, B., Olofsson, P., Loveland, T.R., Jin, S., Dahal, D., Yang, L., Auch, R.F., 2016b. Optimizing selection of training and auxiliary data for operational land cover classification for the LCMAP initiative. ISPRS J. Photogramm. Remote Sens. 122, 206–221. https://doi.org/10.1016/j.isprsjprs.2016.11.004.

Zhu, Z., Wulder, M.A., Roy, D.P., Woodcock, C.E., Hansen, M.C., Radeloff, V.C., Healey, S.P., Schaaf, C., Hostert, P., Strobl, P., Pekel, J.F., Lymburner, L., Pahlevan, N., Scambos, T.A., 2019a. Benefits of the free and open Landsat data policy. Remote Sens. Environ. 224, 382–385. https://doi.org/10.1016/j.rse.2019.02.016.

Zhu, Z., Zhang, J., Yang, Z., Aljaddani, A.H., Cohen, W.B., Qiu, S., Zhou, C., 2019b. Continuous monitoring of land disturbance based on Landsat time series. Remote Sens. Environ. https://doi.org/10.1016/j.rse.2019.03.009. (In press).